SYNTHESIS AND CHARACTERIZATION OF $CuAlO_2$ THIN FILMS BY REACTIVE RF MAGNETRON SPUTTERING

by

Martín Antonio Asmat Uceda

A thesis submitted in partial fulfillment of the requirements for the degree of

MASTER OF SCIENCE
in
PHYSYCS

UNIVERSITY OF PUERTO RICO
MAYAGÜEZ CAMPUS
2010

Approved by:

_____	_____
Héctor J. Jiménez González, PhD Member, Graduate Committee	Date
_____	_____
Surinder P. Singh, PhD Member, Graduate Committee	Date
_____	_____
Maharaj S. Tomar, PhD President, Graduate Committee	Date
_____	_____
Efraín O'Neill Carrillo, PhD Representative of Graduate Studies	Date
_____	_____
Héctor J. Jiménez González, PhD Chairperson of the Department	Date

Abstract

This work presents a comparative study on optical and electrical properties of $CuAlO_2$ thin films on sapphire (0001) substrates deposited with two different growth conditions using reactive RF-magnetron sputtering technique from metallic Cu and Al targets. $CuAlO_2$ is a very promising material for transparent electronic applications, it is intended that comparison of results obtained from both approaches, could lead to optimization and control of the physical properties of this material, namely its electrical conductivity and optical transmittance. All samples were heat treated at 1100°C using rapid thermal annealing with varying time and rate of cooling. The effect of sputtering conditions and different annealing time on phase formation and evolution is studied with X-ray diffraction (XRD) and scanning electron microscopy (SEM). It is found that for most of the samples $CuAlO_2$ phase is formed after 60 min of annealing time, but secondary phases were also present that depend on the deposition conditions. However, pure $CuAlO_2$ phase was obtained for annealed CuO on sapphire films with annealing time of 60 min. The optical properties obtained from UV-Visible spectroscopic measurement reveals indirect and direct optical band gaps for $CuAlO_2$ films and were found to be 2.58 and 3.72 eV respectively. The films show a transmittance of about 60% in the visible range.

Hall effect measurements indicate p-type conductivity. Van der Pauw technique was used to measure resistivity of the samples. The highest electrical conductivity and charge carrier concentration obtained were of $1.01 \times 10^{-1} S.cm^{-1}$ and 3.63×10^{18} cm^{-3} respectively.

Resumen

Este trabajo presenta un estudio comparativo de las propiedades ópticas y eléctricas de películas delgadas de $CuAlO_2$ crecidas en sustratos de zafiro (0001), depositadas con dos condiciones de crecimiento distintas mediante la técnica de RF-magnetron sputtering reactivo a partir de blancos metálicos de Cu y Al. $CuAlO_2$ es un material muy prometedor para aplicaciones en electrónica transparente, se espera que la comparación de los resultados obtenidos por ambas rutas conlleve a la optimización y control de las propiedades físicas del material, en particular su conductividad eléctrica y transmitancia óptica. Todas las muestras se sometieron a tratamiento térmico a una temperatura de 1100°C usando tratamiento térmico rápido con una tasa de enfriamiento variable. El efecto de las condiciones de crecimiento y los diferentes tiempos de tratamiento térmico en la formación y evolución de la fase es estudiada mediante difracción de rayos X y microscopía de barrido electrónico (SEM). Se encontró que para la mayoría de muestras la fase de $CuAlO_2$ es formada luego de 60 minutos de tratamiento térmico, pero fases secundarias estaban presentes dependiendo en las condiciones de deposición. Sin embargo la fase pura de $CuAlO_2$ se obtuvo para las muestras de películas de CuO sobre zafiro con un tiempo de tratamiento térmico de 60 minutos. Las propiedades ópticas obtenidas a partir de mediciones espectroscópicas UV-Visible revelan anchos de banda prohibida directo en indirecto para las películas de $CuAlO_2$ y se halló que sus valores fueron 2.58 y 3.72 eV respectivamente. Las películas mostraron una transmitancia de 60% en la región visible.

Mediciones de efecto Hall indican conductividad de tipo-p. Se utilizó la técnica de Van der Pauw para medir la resistividad de las muestras. La conductividad eléctrica y concentración de portadores de carga más altas obtenidas fueron de $1.01x10^{-1}S.cm^{-1}$ and $3.63\ x10^{18}\ cm^{-3}$ respectivamente.

Dedicatory

To my loved wife, Sol Taina for her inconditional support and company during all this process

To my parents Gerardo and Arlette and to my brothers: Rafael and Denisse, for their enormous strength, inspiration and love.

To my friends, those present and absent.

To every person who has indirectly contributed to this work

Acknowledgements

During the development of my graduate studies in the University of Puerto Rico several persons and institutions collaborated directly and indirectly with my research. Without their support it would be impossible for me to finish my work. That is why I wish to dedicate this section to recognize their support.

I want to start expressing a sincere acknowledgement to:

Dr. Maharaj S. Tomar, because he gave the opportunity and confidence to work in his laboratory.

Dr. Surinder P. Singh for introducing me to this subject, because of his invaluable guidance and orientation. From him I received motivation; encouragement and support during all my research.

Dr. Oscar J. Perales, for his useful insights and ideas that helped me to evaluate things in perspective and for his help with characterization facilities during previous works.

Dr. Héctor J. Jiménez, for enlightening of key physical concepts through his lectures on solid state and statistical mechanics.

Dr. R. Palai and his PhD. Student Javier Wu, for Van der Pauw and Hall Effect measurements.

To Mr. Moreu for his original and professional-leveled technical support.

To Alvaro Instan, for his help in thickness characterization.

To Ramón Díaz, for his valuable help in annealing process.

Table of Contents

Figure List

Figures **Page**

Table List

Tables **Page**

I. Introduction

1. Preamble

Optoelectronics is a key technology area that has contributed in the success of strategic and economic sectors through the advancements in telecommunications, optical storage, solar cells and biomedical applications, and still is one of the most active research fields. Transparent conducting oxides (TCOs) are important materials for optoelectronic devices, because they combine optical transparency in the visible region with controllable electrical conductivity, making possible numerous applications such as functional windows, transparent p-n homojunction, heterojunction, field-effect transistors, etc. Oddly, most of the well-known and extensively used TCOs such as ZnO, ITO, SnO_2 etc. are n-type materials, but the corresponding p-type transparent conducting oxides were missing for a long time. However, recent reports on fabrication of p-type semiconducting TCOs have prompted a renewed interest in these materials [16-17].

Recently, delafossite $CuAlO_2$, $CuGaO_2$, $CuInO_2$, $AgCoO_2$ have emerged as promising p-type transparent oxide semiconductors. $CuAlO_2$ is a transparent p-type semiconducting material that has been predicted to have outstanding potential for use in optoelectronics devices and technology. Thin films of $CuAlO_2$ have been synthesized using different techniques such as pulsed laser deposition (PLD), plasma-enhanced metalorganic chemical vapor deposition (PE-MOCVD), Magnetron Sputtering, etc. Among the deposition techniques, Magnetron Sputtering Deposition (MSD) is widely used because of its versatility and large area deposition capability.

The most important difference between magnetron sputtering process and thermally excited thin-film preparation methods is the higher energy input into the growing film which provides high deposition rates. Furthermore, magnetron sputtering, when compared to other growing technique is characterized by the following advantages: low substrate temperatures, thickness uniformity, good adhesion of film to substrate, easy deposition of alloys and compounds of materials, among others. Therefore, in the present study we have chosen the RF-magnetron sputtering to grow p-type transparent conducting $CuAlO_2$ thin films.

1.1. Research interest in $CuAlO_2$ films

Existing p-type transparent conductors are intensively being investigated. It is imperative to improve their physical properties to match those of n-type, for device applications. The research interest in $CuAlO_2$ films has increased notably during recent years, after the prediction of p-type conductivity [1]. A number of different approaches such as N-doping, oxygen intercalation, co-sputtering, etc. have been used to achieve proper control of electrical and optical properties of $CuAlO_2$ films. However, achieving good quality films with desired physical properties is still a challenge and synthesis process plays a very important role; a systematic study of growth conditions influence on physical properties is lacking. Sputtering technique is one of the inexpensive and large area deposition techniques. Control over the parameters such as partial and total pressure, substrate temperature, target to substrate distance, RF/DC Power, annealing conditions after deposition dictates the physical properties of the material.

In addition, different deposition and annealing conditions must be taken into account because the electrical and optical properties do not depend only upon the stoichiometry of the film but upon the degree of residual stress present in the films.

1.2. Aim of study

The aim of the present work was to study the structure, phase formation and physical properties especially optical and electrical of RF sputtered $CuAlO_2$ thin films and their dependence on growth conditions. To obtain $CuAlO_2$ films with higher degree of transparency and optimal p-type carrier concentrations we have optimized the sputtering growth and post annealing conditions.

1.3. Summary of the following chapters

This document is divided into four sections. Section I corresponds to introductory chapters (1-3). The first chapter provides a presentation and explains the research interest on $CuAlO_2$ films. Chapters 2 and 3 briefly summarize the physical properties of $CuAlO_2$ and the previous experimental reports on deposition of $CuAlO_2$ films respectively and serve as background information for the present work. Methodology is discussed in Section II (chapters 4-7), attention has been given to magnetron sputtering technique and the influence of deposition parameters on the properties of the resulting films. Characterization techniques that are used in this study, namely: (i) X-ray diffraction (XRD), (ii) UV-visible spectrophotometry iii) Electrical properties using Van der Pauw and Hall effect measurements are also discussed in this section.

The experimental results obtained in this study are discussed in detail in section III (chapters 8-11). Finally, the conclusions and suggestions are presented in Section IV.

2. Physical Properties of $CuAlO_2$

2.1. Crystal structure of $CuAlO_2$

Structurally, $CuAlO_2$ belongs to the family of delafossite compounds, named after the mineral $CuFeO_2$ [2]. Delafossite compounds are ternary oxides which have the general formula $A^{(I)}B^{(III)}O_2$, where $A^{(I)}$ represents a univalent noble metal cation (such as Cu^+, Ag^+, Pd^+, etc.) linearly two-fold coordinated to two oxygen ions; and $B^{(III)}$ represents a cation (Al^{3+}, Ga^{3+},Co^{3+}, etc.) nominally in the +3 oxidation sate, octahedrally coordinated by oxides .

These structures are usually described as two alternating planar layers stacked along the c-axis: a layer of A cations in triangular array with no oxygen and a layer of edge sharing BO_6 octahedra originating layer of $[BO_2]$. According to stacking sequence, two polytypes are possible: hexagonal 2H type with P63/mmc space group symmetry and the rhombohedral 3R type with space group symmetry of $R3\bar{m}$ [3-4].

Although $CuAlO_2$ is usually referred as a 3R type delafossite with rhombohedral symmetry [1-5], 2H type $CuAlO_2$ could occur when planar defects are introduced in the crystal structure [6]. As part of delafossite family, $CuAlO_2$ is composed of alternating stacking layers of O–Cu–O dumbbells and edge-sharing AlO_6 octahedral (Al occupying the octahedral interstices) layers. The Cu and Al atoms form alternating layers perpendicular to the c axis. Cu atoms are linearly coordinated by O and the Al atoms are six fold-coordinated with O atoms. The Cu and Al sites in $CuAlO_2$ are surrounded by different local neighborhoods, and as a consequence, have anisotropic crystal structure and properties [7]. Reported lattice parameters for 3R-type $CuAlO_2$

are: a= 2.858 Å, c=16.958 Å and with main bond-lengths: Cu-O=1.861 Å, Al-O: 1.912 Å, Cu-Cu = 2.860 Å [5]. The stacking sequence for delafossite structure of ABO_2 oxides, 3-D and 2-D projection for both 3R and 2H polytypes are shown in Fig. 2.1 below:

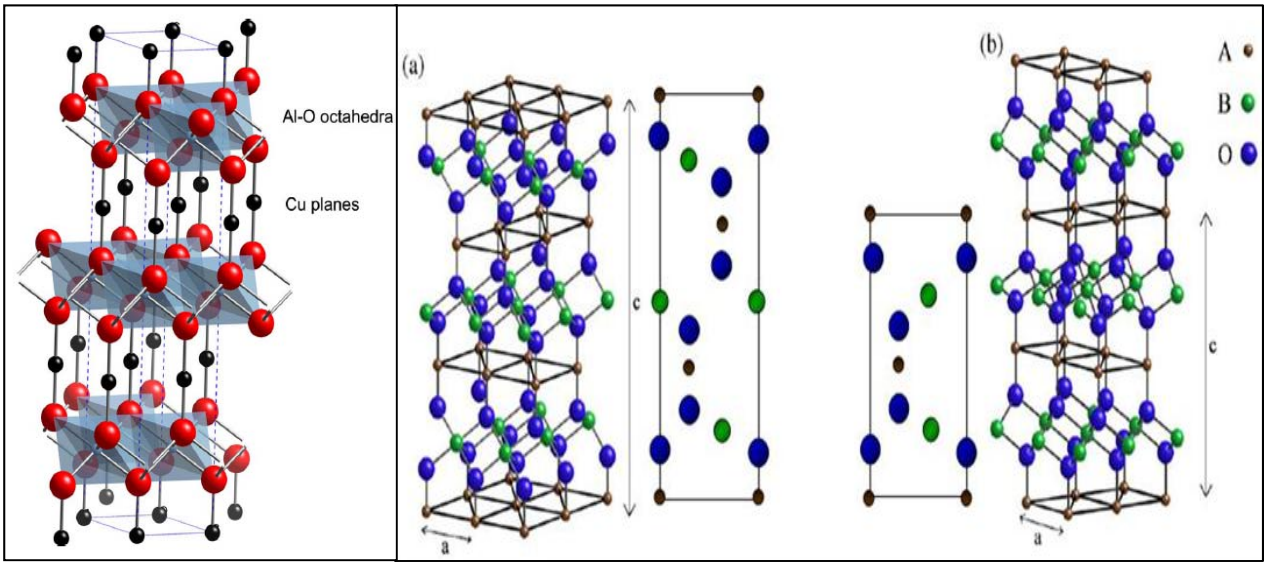

Fig. 2.1 *Delafossite structure of ABO_2 oxides, 3-D and 2-D projection on (1 1 0) plane (a) for 3R polytype (left) and (b) for 2H polytype (right).* Adapted from [¡Error! No se encuentra el origen de la referencia.4,8-9].

2.2. Electrical properties of $CuAlO_2$

$CuAlO_2$ is reported to exhibit p-type conductivity [1]; nevertheless the origin of p-type conductivity for $CuAlO_2$ has not yet been clarified and several models have been proposed. Tate et al. [9] suggested that holes are thermally activated from copper-vacancy acceptor states located about 700 meV above the valence-band maximum giving rise to p-type nature of $CuAlO_2$. Some of the models proposed for $CuAlO_2$ include variable-range hopping [10, 11], band-conduction, [12] and small polaron transport [1,13].

The stacking of AlO_2-Cu-AlO_2-Cu in $CuAlO_2$ plays a key role on its electrical properties. Electrical conductivity is markedly anisotropic for delafossites: up to 25 times higher in the plane perpendicular to the c axis than along that axis, [9,10]. Cu cations when forming part of this structure have a low coordination number, suggesting strong repulsions between 2p electrons from oxide ions and d^{10} electrons on Cu cations [12]. In the AlO_2 layer, the distance between two neighboring Al cations in the same layer is short, and there are no intervening oxygen atoms on the line connecting the Al cations, opening a possibility for n-type conductivity suggesting the formation of transparent homojunctions.

From the point of view of applications and technology, it is desirable to increase conductivity of $CuAlO_2$ to values of at least the same order of magnitude as of n-type transparent conductors. Enhanced p-type conductivity has been reported for $CuAlO_2$ thin films annealed in oxygen-rich environments, [11, 14]. Some authors [15, 16], have suggested that films prepared by Kawazoe [17] obeys the chemical formula $CuAlO_{2+x}$ with as low as 0.001 at% of excess oxygen over stoichiometric value. However, the diffusion mechanism of oxygen in $CuAlO_2$ is not clear. When comparing the reported electrical properties for thin films, it must be taken into consideration that grain boundaries, strain and other defects, common in thin films also affect the resulting electrical measurements.

The electrical conductivity and other electrical properties are very sensitively on the deposition conditions and especially on the annealing process. Table 2.1 summarizes some of the reported electrical properties for $CuAlO_2$ thin films deposited with different techniques in recent years.

Table 2.1. *Reported electrical properties for $CuAlO_2$ thin films*

Technique	Conductivity ($S\ cm^{-1}$)	Carrier density (cm^{-3})	Hall coeff. ($cm^3\ C^{-1}$)	Hall mobility ($cm^2\ V^{-1}s^{-1}$)	Reference
PLD	9.5×10^{-1}	1.3×10^{17}	+48.6	10.4	[12]
DC Sputtering	5.1×10^{-1}	3.5×10^{17}	-	9.4	[18]
RF Magnetron Sputtering	2.6×10^{-3}	3.4×10^{16}	+183.6	4.07	[19]
RF Magnetron Sputtering	1.6×10^{2}	2.61×10^{16}	-	3.81	[20]
DC Magnetron Sputtering	3.9×10^{-1}	1.2×10^{18}	+4.60	-	[21]

2.3. Electronic properties of $CuAlO_2$

Buljan et al. [22], published one of the first calculations of the electronic band structure of $CuAlO_2$. By employing Hartree-Fock method they found that the energy gap was of indirect type with values of 11.65 and 11.78 eV for 2H and 3R $CuAlO_2$ polytypes, respectively. Evaluating density of states (DOS), they established that valence band is predominantely dominated by Cu 3*d* states while 4*p* states contribution is negligible; however they found a small contribution of 4*s* states in agreement with the s - d_z^2 Orgel hybridization model for linearly coordinated Cu^+ ions. Valence band presented also contribution from O 2*p* states overlapped with sharp Cu 3*d* states. Later, Yanagi et al. [11] by comparing measurements of normal and inverse photoelectron spectroscopy (PES/IPES) and using full potential linearized augmented plane wave method (FLAPW) also evaluated band structure of $CuAlO_2$, shown in Fig 2.2. As can be seen from the graph, the calculated band gap of $CuAlO_2$ was of indirect type, with the valence band maximum (VBM) located at the **F** point, while the conduction band minimum (CBM), was at the **Γ** point. The calculated direct gap (**Γ** – **Γ** transition) was 2.8 eV and the indirect gap (**F**- **Γ** transition) was

1.7 eV, while the experimental values they obtained were of 3.5 and 1.8 eV for the direct and indirect band gap, respectively.

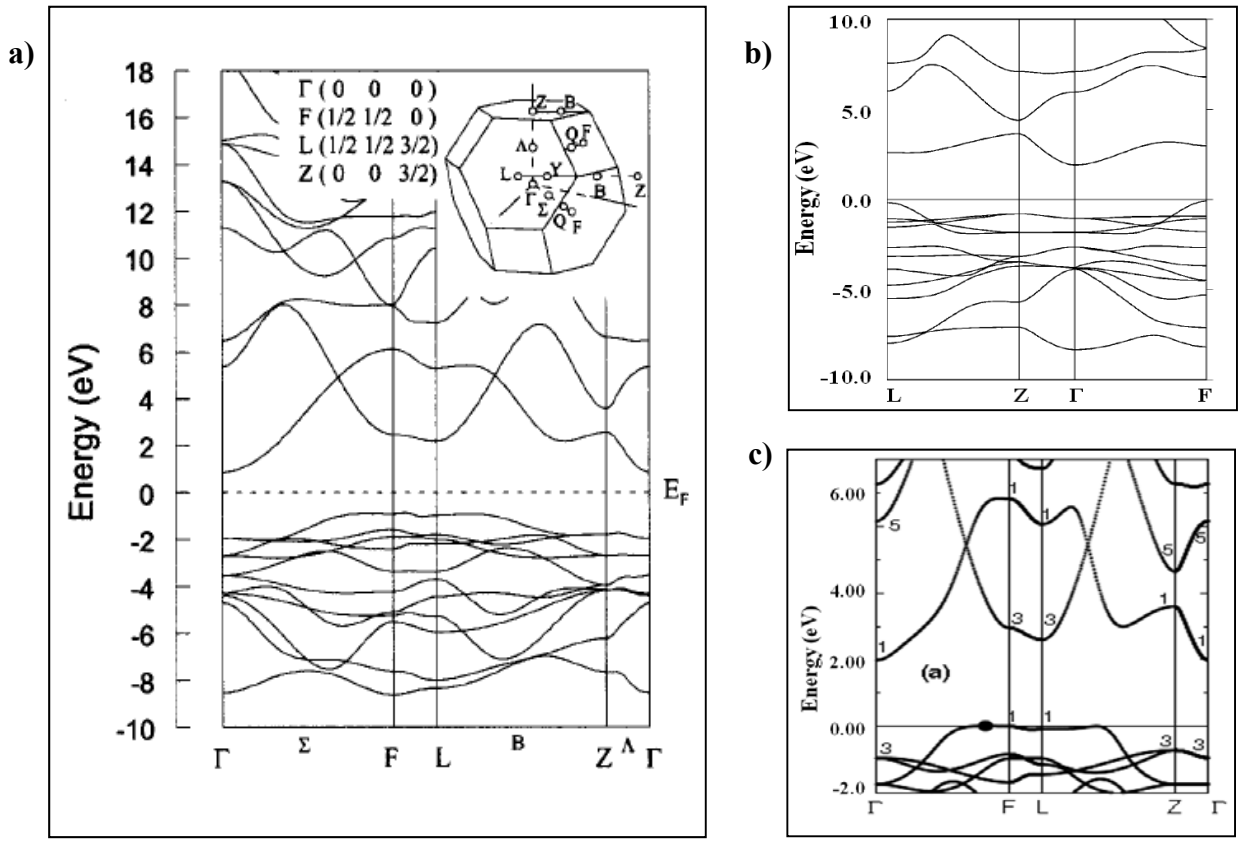

Fig 2.2 *Band Structure of $CuAlO_2$ calculated by using FLAPW method by:* ***a)*** *Yanagi et al.*[11]*,* ***b)*** *Ingram et al.* [13] *(Adapted),* ***c)*** *Nie et al.* [23] (Adapted).

In addition, from the partial density of states (PDOS), they also found that the upper valence band is mainly composed of admixed state of Cu 3*d* and O 2*p* orbitals while Al 3*p* states contribution is negligible.

Ingram et al. [13], found an indirect gap from **Γ** to **F** of 1.95 eV and a direct optical gap of 2.7 eV, however the lowest conduction band was relatively flat as can be seen in Fig 2.2. Nie et al [23], in contrast, determined that the fundamental gap is located at point **L** instead of **Γ** see fig 2.2. with a value of 2.68 eV, and that direct transition between $\mathbf{\Gamma_{val}}$ and $\mathbf{\Gamma_{cond}}$ was forbidden.

Further calculations and refinements of the electronic band structure can be found in the literature; [24,25] although there is a qualitative similarity among most of them, there are also important discrepancies and more studies are needed.

2.4. Optical Properties of $CuAlO_2$

Optical properties of $CuAlO_2$ have tremendous importance because of its possible application for optoelectronic technology, so high transparency in the visible spectrum is desirable. Fig 2.3 shows a UV-visible-NIR transmittance spectrum for reactive DC sputtered thin films. [26]

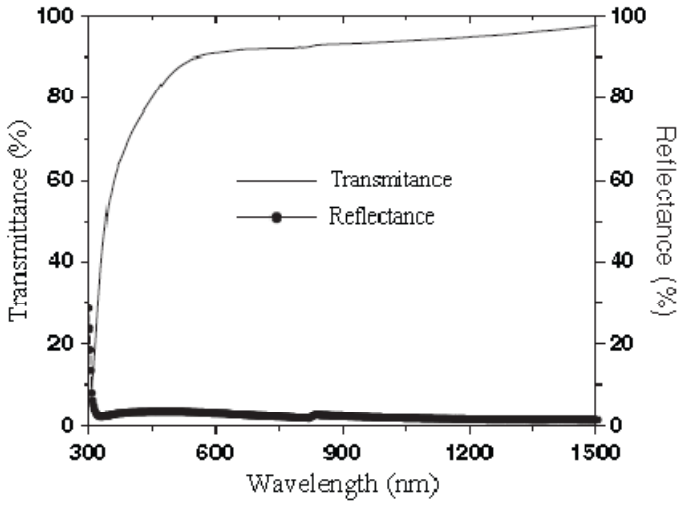

Fig. 2.3 *Optical transmittance and reflectance of $CuAlO_2$ thin film* [26].

Although Fig. 2.3 corresponds to a high transparent sample, most typical values are in the range of 40 - 80% for optical transmittance.

The indirect and direct allowed optical band gaps values also depend on the growing technique employed; e.g., Cai et al. [27] found that variation of Cu/Al ratio of $CuAlO_2$ produced

a variation in optical properties, and higher Cu/Al ratio produced increment of direct band gap from 2.9 to 3.6 eV. Some of the values reported are in the range of 1.8-2.8 and 3.5-3.9eV, for the indirect and direct band gap respectively [11, 14, 28-29].

2.5. Phase Diagram of $CuAlO_2$

Phase diagrams are graphs showing the limiting conditions such as pressure, temperature, etc. at which one or more phases can exist in thermodynamical equilibrium. Phase diagrams constitute a very useful tool when preparing compound materials. Although, there could be significant differences in the phase diagram for thin films with respect to those for bulk material, they provide a starting point to determine the conditions at which deposition and annealing processes could be done.

The Phase diagram for CuO-Al_2O_3 was investigated by Misra [30] and is shown in Fig. 2.4. In this diagram, it can be observed that copper aluminates $CuAl_2O_4$ and $CuAlO_2$ will form at temperatures above 800 °C.

The range 900° - 1000°C was excluded from the graph (Fig. 2.4) however, according to these results, the compound $CuAl_2O_4$ is formed at 800 °C and is stable to a maximum temperature of 1000 °C in air, and then it is converted into $CuAlO_2$ which is stable at about 1260°C in air.

From the diagram, it can be observed that $CuAlO_2$ is formed according to peritectic reaction, that is, a liquid and solid phase of fixed proportions react at a fixed temperature to yield a single solid phase. In this case we would have: $Cu_2O_{(l)} + Al_2O_{3(s)} \rightarrow 2\ CuAlO_{2\ (s)}$

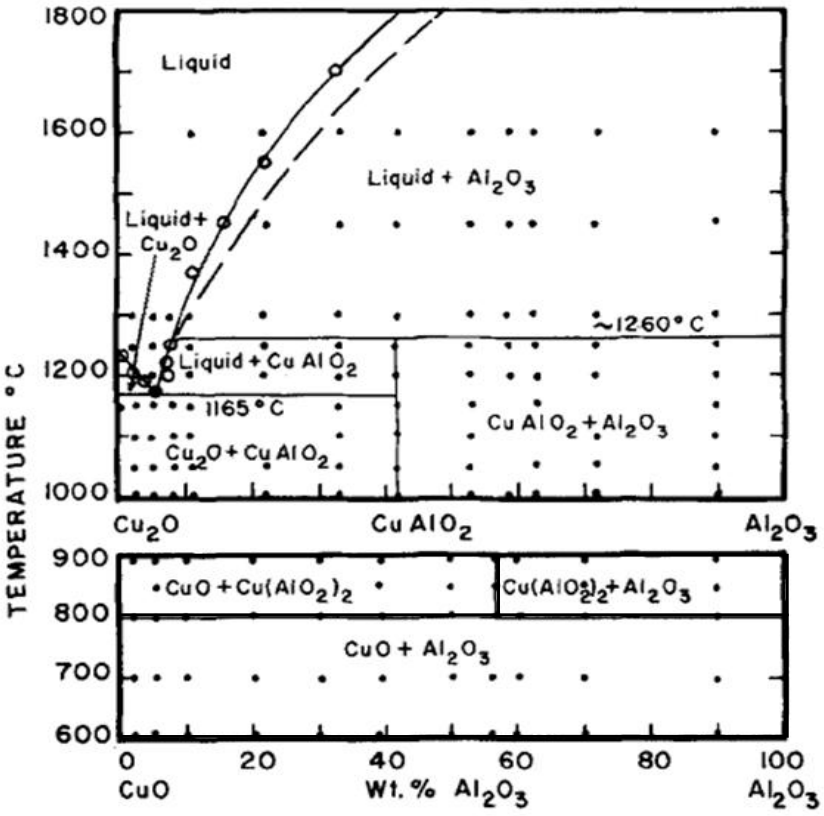

Fig. 2.4 *Phase Diagram for CuO-Al_2O_3* [30]

Jacob and Alcock [31] have studied the thermodynamics of $CuAlO_2$ and $CuAlO_4$ and determined their standard Gibbs free energies of formation in the range of 700 – 1100 °C. They deduced the chemical reaction formula for the formation of $CuAlO_2$ and $CuAl_2O_4$ as follow:

$$2Cu_2O + O_2 \rightarrow 4CuO, \Delta G^\circ = -62,354 + 44.89T(\pm 100)$$

$$4Cu + O_2 + 2Al_2O_3 \rightarrow 4CuAlO_2, \Delta G^\circ = -91,510 + 39.21T(\pm 300)$$

$$Cu_2O + Al_2O_3 \rightarrow 2CuAlO_2, \Delta G^\circ = -5,670 + 2.49T(\pm 300)$$

$$4CuAlO_2 + 2Al_2O_3 + O_2 \rightarrow 4CuAl_2O_4, \Delta G^\circ = -33,400 + 20.02T(\pm 300)$$

$$CuO + Al_2O_3 \rightarrow CuAl_2O_4, \Delta G^\circ = 4,403 - 4.97T(\pm 350)$$

3. Review of Previous experimental reports

$CuAlO_2$ is a compound known to exist for more than 50 years [2]. The first report of its p-type conductivity was published in 1984 by Benko et al. [1], however after 1997, when Kawazoe's group prepared it in transparent thin films form for the first time [17], there has been a growing interest on this material for possible applications in p-TCO technology, as evidenced by the number of publications on the subject. Kawazoe et al. reported highly transparent thin film of delafossite copper aluminum oxide ($CuAlO_{2+x}$), deposited by PLD technique, and a room temperature p-type conductivity of $9.5x\ 10^{-1}$ S cm^{-1}. This high conductivity of almost 1 S cm^{-1}, was 3 to 4 orders of magnitude smaller than that of n-type conducting indium–tin oxide (ITO), however, the observed Hall mobility of 10 $cm^2V^{-1}\ s^{-1}$ was comparable to that of ITO and as high as a polycrystalline thin film of an ionic crystal with wide band gap. Substitutional doping for increasing the hole concentration of thin film from $1.3x10^{17}$ cm^{-3} to the order of 10^{20} cm^{-3} was suggested in the mentioned report [17].

Up to now $CuAlO_2$ thin films have been synthesized using different techniques. A brief review of the most relevant work on deposition of such thin films is presented.

3.1. Deposition techniques

The usefulness of each deposition technique depends on their specific capabilities and limitations. Deposition techniques for $CuAlO_2$ thin films include:

- Pulsed laser deposition [11-12],[17],[32-35]
- Sputtering deposition [15], [18-21], [26], [36-47]
- Chemical Vapor Deposition [14],[27], [48-49]

- Spray Pyrolysis [50-51]
- Sol Gel [52-53]
- Microwave irradiation [54]
- Wet oxidation [55-56]

Efforts have also been made on the preparation of $CuAlO_2$ single crystals [5,29,57-58], however because compounds containing Cu^+ melt incongruently at high temperature, the resulting $CuAlO_2$ sample was difficult to pull out from the melt and leaching in hot HNO_3 for many days was required [9]. The mostly used techniques for depositing $CuAlO_2$ films are Pulsed Laser Deposition (PLD) and Magnetron Sputtering Deposition (MSD). The present work suggest that parameters such as annealing time and cooling rate, if controlled properly, could lead to films with improved optical transmittance and electrical conductivity.

3.2. Deposition of $CuAlO_2$ films by Pulsed Laser

Pulsed laser Deposition (PLD) is a sophisticated technique commonly employed for deposition of thin films. Kawazoe's work [17] entitled "*P-type electrical conduction in transparent thin films of* $CuAlO_2$" started and stimulated an interest in deposition of $CuAlO_2$ films and in particular by employing pulsed laser technique. In that work, a 248nm, 20Hz and 200 $mJcm^{-2}$ KrF excimer laser was used as energy source to create plasma plume to deposit $CuAlO_2$ films on a single crystalline (0001) sapphire substrate at a temperature of 700 °C and deposition pressure of 100 mTorr , no information about post-deposition thermal treatment was presented. Many other authors have successfully used this technique to prepare $CuAlO_2$ thin films. Table 3.1 summarizes the principal deposition parameters and properties of films deposited by using PLD technique.

Table 3.1 *Synthesis conditions and physical properties of $CuAlO_2$ films deposited by PLD*

	Autor & Year	Kawazoe, 1997	Yanagi, 2000	Deng, 2008	Díaz, 2009
Deposition	**Target**	$CuAlO_2$ sintered	$CuAlO_2$ sintered	$CuAlO_2$ sintered	$CuAlO_2$ sintered
	Substrate	Sapphire (0001)	Sapphire (0001)	Sapphire (0001)	Sapphire (0001)
	O_2 pressure (mTorr)	100	9.7 mTorr	2-3.5 x10-2 Pa	10
	Temperature (°C)	700	700	400-600	700
Post Deposition Annealing	**Temperature (°C)**	-	700	500 – 900	1050
	Time (h)	-	3	1	-
	Atmosphere	O_2	O_2	N_2	O_2
Properties	**DC conductivity (S cm^{-1})**	9.5 $x10^{-1}$	3.4 $x10^{-1}$	1.0$x10^{-2}$	1.7$x10^{-2}$
	Hall Coefficient (cm^3C^{-1})	48.6	+0.23	-	-
	Carrier concentration (cm^3)	1.30$x10^{17}$	2.7$x10^{19}$	-	-
	Hall mobility ($cm^2V^{-1}s^{-1}$)	10	0.13	-	-
	Reference	**[17]**	**[11]**	**[16]**	**[59]**

3.3. Deposition of $CuAlO_2$ films by Magnetron Sputtering

Most of the works on $CuAlO_2$ films deposition by magnetron sputtering share certain common characteristics, such as the use of reactive gas for deposition, Ar/O_2 mixture ratio and annealing after deposition of the films. The variations have been reported through the choice of DC or RF Power Source for deposition, the use of ceramic Cu-Al target (including $CuAlO_2$ target) or metallic Cu and Al targets and specific method of deposition such as Co-Sputtering, Sequential sputtering (multilayers), or direct deposition of the films. It is noteworthy that the substrate plays an important role in the resulting characteristics of the films. Substrates which can hold high temperature annealing steps to achieve proper phase formation are required, where sapphire is the most suitable. Other very important factor for good quality films is the annealing conditions after deposition, such as heating/cooling rate, annealing time and annealing atmosphere. Table 3.2. shows the experimental conditions for the deposition of $CuAlO_2$ by magnetron sputtering in the past.

Table 3.2. *Previous Works on $CuAlO_2$ thin films using magnetron sputtering*

Author and year	Power, Source Type	Precursor Target	Substrate	Deposition Temperature (° C)	Deposition Gases Ratio	Deposition Pressure (mTorr)	Annealing Atmosphere	Annealing Temperature (° C)	Reference
Reddy, 2009	DC	Cu-Al alloy	Glass	30-375	Not reported	45	Not Reported	Not Reported	a el origen de
Lan, 2009	100W RF	$CuAlO_2$ ceramic	quartz	Room Temperature	4:1, Ar:O_2	Not Reported	Air, N_2	700-1000	[19]
Dong, 2009	100W RF	$CuAlO_2$ ceramic	quartz	500	3:2, Ar:O_2	3.8-30	Vacuum, N_2	500-900	[20]
Tsuboi, 2008	7.5W Cu, 21W Al DC	Cu, Al metallic	Sapphire (0001)	500-680	4:1, Ar:O_2	4	N_2	1050	[46]
Shy, 2008	RF	Cu, Al metallic	Sapphire (0001)	Room Temperature	Ar, O_2 4%	5	Air, N_2, O_2	1000, 1100	[42]
Singh, 2008	DC	Cu, Al metallic	Sapphire (0001)	Not reported	Not Reported	4.5	Not Reported	Not Reported	[43]
Yu, 2007	150W DC	Cu-Al alloy	quartz	Not reported	3:1, Ar:O_2	6.5	Ar/O_2	800	[47]
Tsuboi, 2007	7.5W Cu, 21W Al DC	Cu, Al metallic	Sapphire, quartz	500-700	4:1, Ar:O_2	4	N_2	1050	[45]
Banerjee, 2005	12W DC	$CuAlO_2$ ceramic	Si, glass	180	3:2, Ar:O_2	1.5	O_2	200	[15]
Ong, 2003	100W RF	Cu, Al metallic	Glass	100	Ar, O_2 5%	Not Reported	Not Reported	Not Reported	[40]

Shy et. al. [41-42] have reported the synthesis of $CuAlO_2$ films by sputtering using sequential deposition of Cu_2O and Al_2O_3 on sapphire substrate at room temperature. For the precursor films, metallic Cu and Al targets were used, with the advantage of compositional high purity of the targets. The oxides were obtained by using a reactive Ar/O_2 atmosphere during film formation. A schematic of the process is shown in Fig. 3.1.

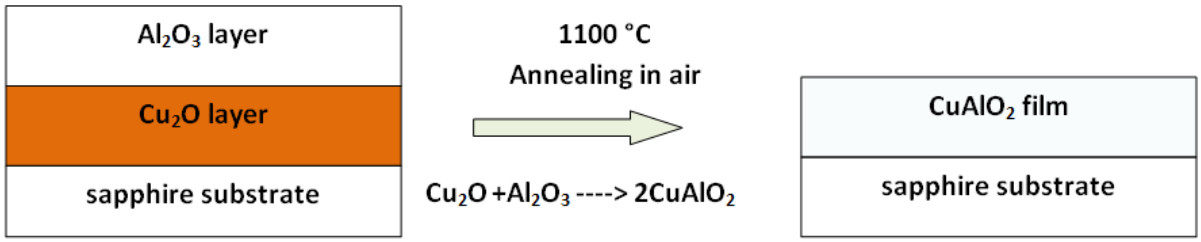

Fig. 3.1 *Schematic of sandwich structure of Al_2O_3/Cu_2O/sapphire before and after annealing.* Adapted from [41]

They have investigated the effect of the annealing conditions such as cooling/heating rate and temperature. It was found that temperature higher than 1000 °C was required for proper phase formation of $CuAlO_2$ in air atmosphere, and that slow cooling rate is favorable to obtain better crystallinity in the films. Oxygen content in the annealing ambient affected the phase formation, and annealing in pure oxygen led to the formation of $CuAl_2O_4$.

The role of the annealing conditions on the $CuAlO_2$ have also been studied and reported by other groups [7,19]. Yu et. al [19] studied the relaxation behavior of N doped and un-doped $CuAlO_2$ films after annealing at different conditions. They found a strong dependence of the relaxation behavior of the residual stress on the structural and atomic configuration of delafossite $CuAlO_2$. They showed that the polycrystalline $CuAlO_2$ would first undergo phase transformation, and subsequently CuO hillocks would be formed in order to release the high

compressive residual stress, as is shown in Fig. 3.2 for N-doped $CuAlO_2$ films (the compressive residual stress increased after N doping).

This tendency to form CuO hillocks was attributed to difference in bonding energies of the constituent atoms: the bonding energy of one Cu-Cu pair in a Cu layer is about 30 times weaker than the Cu-O pair and the Al has the highest total bonding energy value. A schematic of the delafossite structure of $CuAlO_2$ in which the Cu and O atoms diffuse along the plane perpendicular to the c-axis is shown in Fig. 3.3.

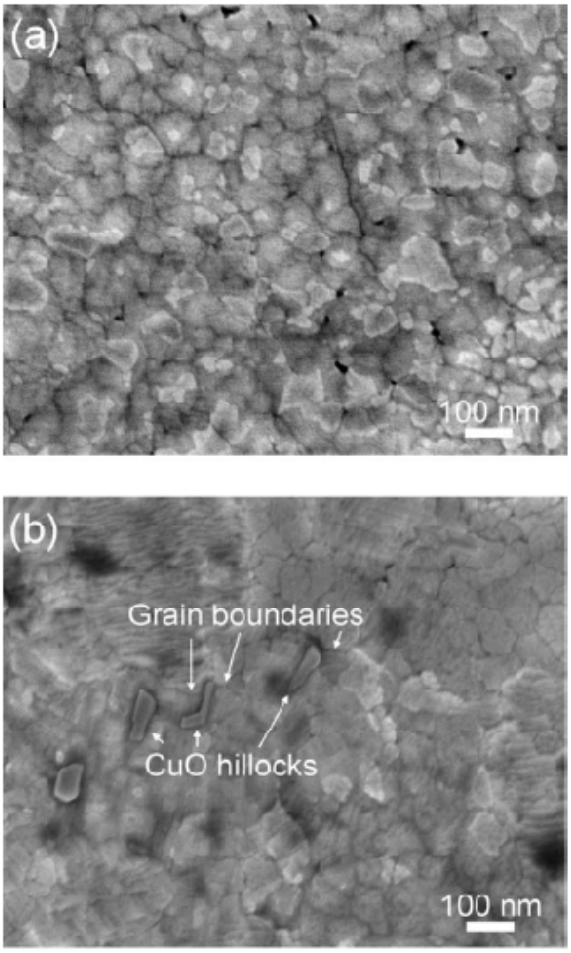

Fig. 3.2. *FESEM images of 800 °C annealed films grown on silicon substrate:* **(a)** *Undoped, and* **(b)** *N-doped $CuAlO_2$ film* [7]

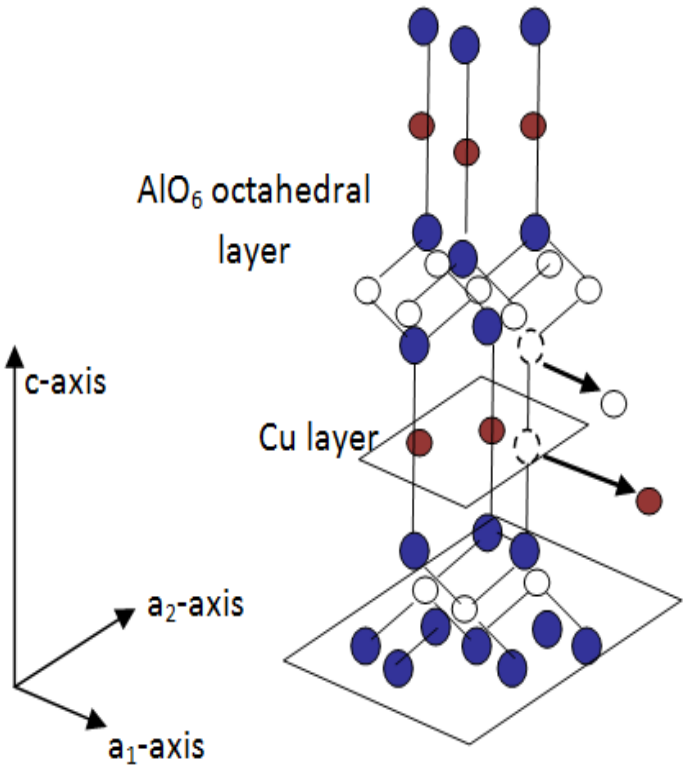

Fig. 3.3. *Schematic of diffusion of Cu and O atoms along the a-axis direction of the close-packed Cu layer while under compressive stress* [7]

3.4. Influence of Sputtering Parameters

Since sputtering is a physical deposition process in vacuum, several parameters could affect the deposition and film properties.

3.4.1 Influence of Deposition Pressure:

Dong et al [20] have studied the effect of gas pressure during deposition of $CuAlO_2$ films on the structural, optical and electrical properties of the films. In their work, a mixture of Ar and O_2 gases were used in a proportion of 3:2, while the working gas pressure was varied from 0.5 - 4.0 Pa (3.76 - 30.0 mTorr). From XRD characterization, they found that the crystalline orientation of the films depends on the deposition pressure: by decreasing the pressure, the intensity of the peak corresponding to (101) diffraction plane decreases, whilst the intensity of the (003) and (006) peaks increases evidencing c-axis orientation. This preferred orientation would also favor electrical conduction in the film [10, 39]. Electrical and optical properties were also susceptible to the working pressure as shown in Table 3.3:

P_w (Pa)	0.5	1.0	2.0	3.0	4.0
Direct band gap (eV)	3.54	3.6	3.5	3.55	3.66
Indirect band gap (eV)	1.92	2.03	1.89	1.95	2.10
Activation energy (eV)	0.043	0.065	0.062	0.059	0.078
Conductivity ($x10^{-2}$ Scm^{-1})	1.6	1.35	1.1	0.82	0.68
Carrier conc. ($x10^{16}$ cm^{-3})	2.61	2.76	2.65	2.82	3.17
Mobility ($cm^2V^{-1}s^{-1}$)	3.81	3.05	2.60	1.81	1.34

Table 3.3 *Pressure effect on optical and electrical parameters of $CuAlO_2$ films.* Data taken from [20]

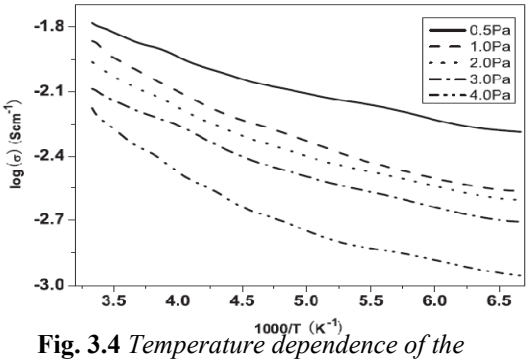

Fig. 3.4 *Temperature dependence of the conductivity of $CuAlO_2$ with pressure* [20].

It is interesting to be noted that carrier concentration increases slightly with increasing pressure. This effect was attributed to the increasing of interstitial oxygen content which could be the origin of the positive holes and consequently of p-type conductivity. However a higher

conductivity of $CuAlO_2$ films corresponds to lower working pressure P_w as can be seen in Fig. 3.4. The authors explained that electrical conductivity is highly anisotropic and the c-axis orientation tendency found with decreasing pressure is in concordance with increasing conductivity.

3.4.2 Influence of Annealing Parameters

The annealing parameters play a key role in the phase formation and physical properties of $CuAlO_2$. Lan et al. [19] have carried out annealing of samples in N_2 ambience at temperatures of 700-1000 °C. They reported that for temperatures lower than 900 °C, $CuAlO_2$ phase with a (015) preferred orientation is obtained, and for temperature of 900 °C, highly crystalline c-axis oriented $CuAlO_2$ phase is obtained, as evidenced by XRD and Raman Scattering characterization (figs. 3.5 and 3.6). At that temperature, they have also carried out annealing in air atmosphere, and as a result secondary $CuAl_2O_4$ and CuO were found in addition to $CuAlO_2$, suggesting that N_2 would constitute a protective atmosphere that avoids decomposition of $CuAlO_2$.At higher temperatures, weakened crystallinity is observed, correlated to appearance of microscopic cavities in the films.

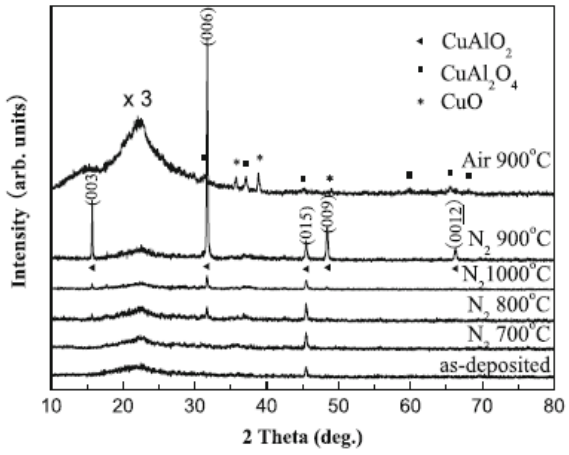

Fig. 3.5 *XRD Patterns of $CuAlO_2$ films as-deposited and annealed in N_2 ambience at different temperatures* [19].

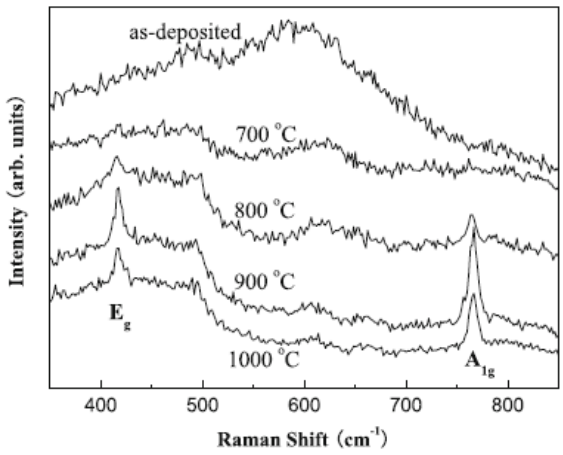

Fig. 3.6 *Raman scattering spectra of $CuAlO_2$ films as-deposited and annealed in N_2 ambience at different temperatures* [19].

II. Methods and Experiments

4. Magnetron Sputtering Deposition

Magnetron Sputtering is a flexible technique used to coat a wide range of materials, any solid metal or alloy and a variety of compounds. The sputtering process has almost no restrictions in the target materials, ranging from pure metals (where a D.C.-power supply can be used) to semiconductors and isolators (which require a RF-power supply or pulsed dc). Deposition can be carried out in either non reactive (inert gas only) or reactive (inert and reactive gas) discharges with single or multi-elemental targets.

4.1. Basics of Magnetron Sputtering Deposition

Magnetrons are diode sputtering sources in which magnetic fields are used with the cathode surface to form electron traps which are so configured that $\vec{E}x\vec{B}$ electron drift currents close themselves. ($\vec{E}$ = Electric field, $\vec{B}$ = Magnetic field).

Sputtering is categorized as a physical vapor deposition (PVD) technique. Sputtering involves the removal of atoms from "target", due to energetic bombardment of its surface layers by ions of an inert gas (usually argon). It is performed by applying an external electric field across the anode and cathode in the presence of inert gas to produce a plasma state. In this condition, ions of the gas are accelerated towards the target by a DC or RF voltage bias. Subsequent to the erosion of atoms from the target, formation of a layer of the extracted material on the substrate takes place. Prior to the sputtering procedure a base pressure of 10^{-6} torr is

required to get rid of any impurity from environment. The deposition pressure usually is 10^{-2} to 10^{-3} Torr depending upon the material to be deposited and phase to be required, and is achieved through the introduction of inert gas such as argon.

In magnetron sputtering, during the sputtering process a magnetic field allows to trap secondary electrons to a region close to the target. This improves the deposition rate by maintaining a higher density of ions, which makes the electron/gas molecule collision process much more efficient. For achieving this, powerful magnets with alternating polarity are arranged behind the target, this configuration constitutes a magnetron and hence the name Magnetron Sputtering.

The electrons follow helical paths around the magnetic field lines undergoing more ionizing collisions with neutral gaseous near the target than would otherwise occur. This enhances the ionization of the plasma near the target leading to a higher sputter rate. This is shown in Fig. 4.1.

It also means that the plasma can be sustained at a lower pressure. The sputtered atoms are neutrally charged and so are unaffected by the magnetic trap. When power is supplied to a magnetron a negative voltage is applied to the target attracting positive ions to the target surface at a given speed. Generally when a positive ion collides with atoms at the surface of a solid an energy transfer occurs. A surface atom becomes sputtered if the energy transferred to it, normal to the surface, is larger than about 3 times the surface binding energy (approximately equal to the heat of sublimation). The resulting crystallographic phase of the film depends on the substrate type, its temperature and the surrounding atmosphere

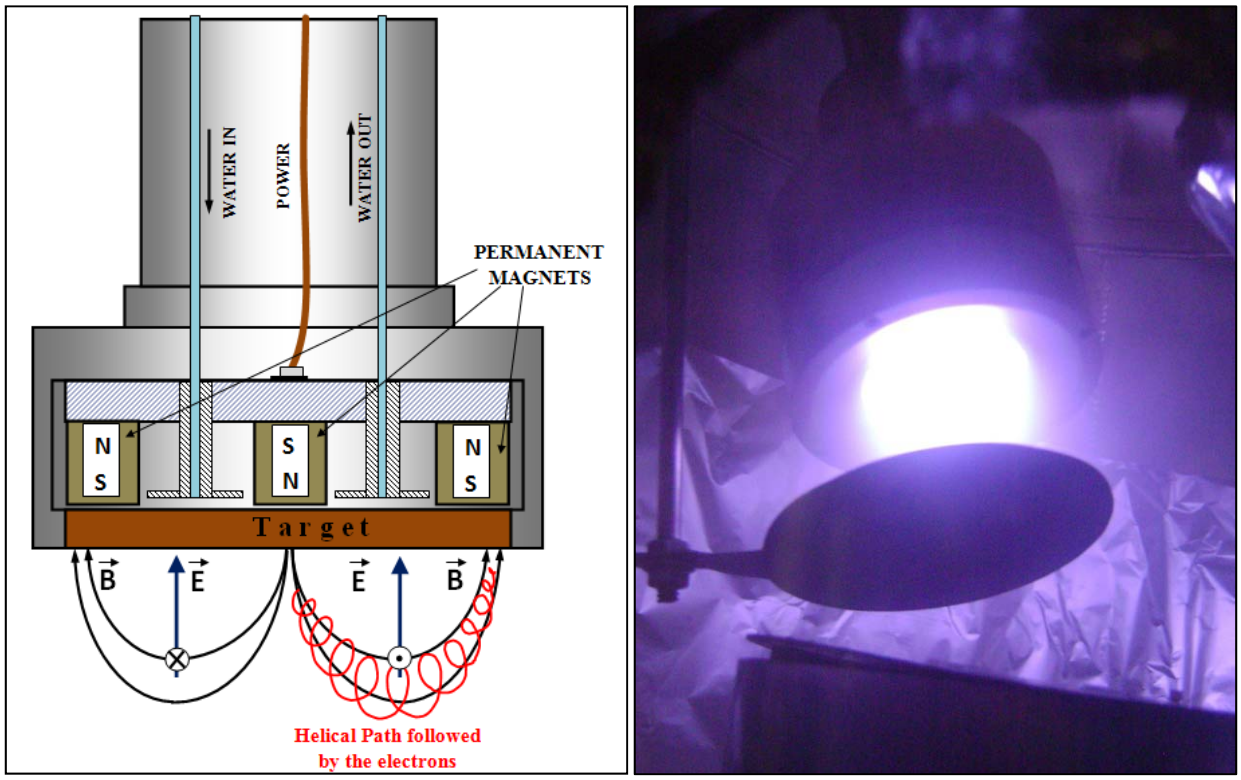

Fig. 4.1 ***Left****: Diagram of magnetron sputtering showing the direction of the magnetic and electric field,* ***E*** *and* ***B*** *as well as the resulting direction of the electrons under influence of those fields.* ***Right****: deposition process by magnetron sputtering where the glowing plasma can be observed confined to a region near to the sputtering target.*

4.2. Reactive RF-Sputtering

Sputtering deposition is carried out under an inert gas ambient such as Ar, and then it is called Non-Reactive Sputtering. Simplest sputtering requires minimum process control [60]. Reactive gas, (O_2/N_2/CH_4, etc.) is added during sputtering, with the intention of forming compounds (such as oxides, nitrides, borides, carbides, etc.) from the metallic targets and then it is called ***Reactive Sputtering***.

Reactive sputtering has significantly different characteristics than non-reactive sputtering process, one of the principal effects of adding reactive gas is that sputter rates of metals drops dramatically; this is known as "poisoning" and is usually due to the fact that a compound (usually oxides, if adding O_2) is formed on the surface of the target exposed to the reactive gas;

hysteresis is observed in the processing curve for film deposition rate vs. flow of the reactive gas [61], as showed in the Fig 4.2.

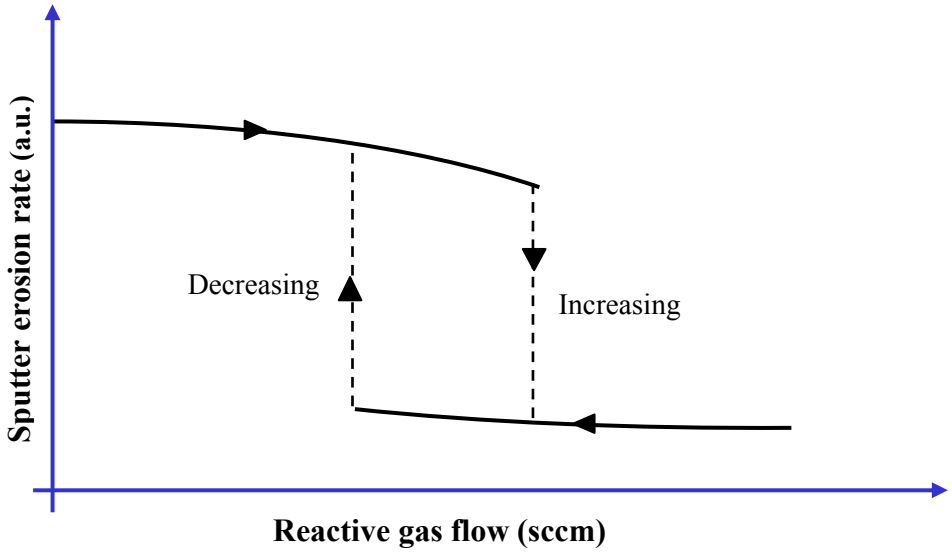

Fig. 4.2 *Typical experimental hysteresis curve for reactive sputtering.* Adapted from [60]

Generally DC sputtering is used when dealing with conductive materials or alloys from conductive targets while RF sputtering is more common in deposition of semiconductors and isolators, and sometimes a combination of both is also used. [61-62]

4.3. Experimental considerations

In order to obtain $CuAlO_2$ thin films starting from metallic Cu and Aluminum targets, a set of different combinations are possible within RF sputtering technique depending on the gas employed (Reactive or Non-reactive gas) and the type of sputtering deposition (co-sputtering, direct deposition, alternating layers deposition). Reactive sputtering was used in this work for preparing $CuAlO_2$ thin films by ***1)*** direct deposition of CuO, and ***2)*** sequentially deposited CuO and Al_2O_3 films on sapphire substrates. In both cases rapid annealing was employed for proper phase formation of $CuAlO_2$.

The scheme of the experiment proposed for this work is illustrated in Fig 4.3.

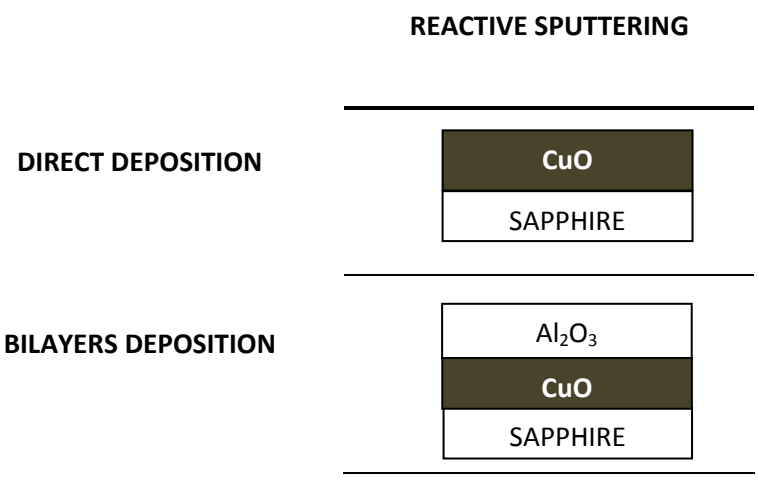

Fig. 4.3 *Schematic of layered deposition of CuO and Al_2O_3 films in this work.*

RF sputtering was chosen instead of DC sputtering due to the fact that deposition of Al_2O_3 was somewhat difficult when using metallic target. When oxygen was added to the chamber for deposition of Al_2O_3, DC Power (both voltage and current) dropped to approximately a third part of its value, and voltage turned fluctuating in a range of $\pm$ 10W. Even, by manual stabilization of the voltage, deposition rate was poor compared to Al. This effect was attributed to the "poisoning" phenomena, discussed in the previous chapter: when oxygen is added, a thin film of Al_2O_3 is formed onto the surface of the Al target, thus could favor arcing, hysteresis phenomena, inhomogeneities and poor deposition rates [63-64].

4.3.1. Magnetron sputtering system setup

The magnetron sputtering system used in this work possesses a configuration on-axis with two magnetron sputter guns for two modes sputtering process: direct current (DC) and radio frequency (RF) magnetron. Fig. 4.4 depicts a complete schematic of the magnetron sputtering system.

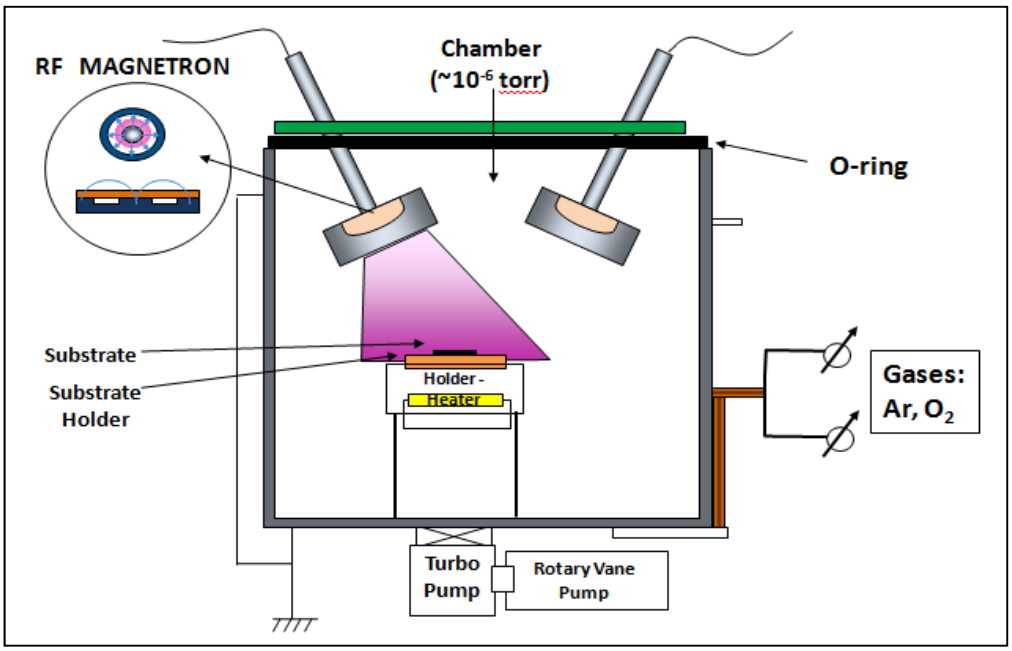

Fig. 4.4 *Schematic diagram of Magnetron sputtering system*

The process chamber is cylindrical in shape with dimensions of 16″ diameter x 16″ high, made of 394-grade stainless steel. It has a full opening top plate for easy access to all internal components – the guns for changing targets, substrate stage for loading and unloading samples.

Both guns have a diameter of 2″ and are implemented with shutters on the plate at an approximate angle of 65 degrees. These guns can be adjusted linearly in order to vary the distance between the substrate and the guns. The sputtering process can be visually monitored with an additional 4″ view port placed in the front of the chamber. In addition, the chamber has two view ports on the sides at 70 degrees intended to monitor the substrate and film evolution with ellipsometric measurements. A photograph of the sputtering deposition equipment used for the present work is shown in Fig 4.5.

This equipment has a vacuum pumping system consisting of a Varian 200 l/s turbo molecular pump, a two stage direct drive rotary vane mechanical pump and a 4″ manually operated stainless steel gate valve that bring access to the working chamber.

Fig. 4.5 *Sputtering system setup used of this work.* (Dr. M. S. Tomar's Laboratory, UPR-M)

The system has two gas inlets (one for oxygen, the other for argon) controlled by needle valves. Vacuum is monitored by employing a cold cathode combination gauge (760 – 10^{-8} Torr). A stainless steel substrate holder capable of mounting up to 4″ diameter wafer/sample is provided. This holder is capable of being heated up to a maximum temperature of 400 degree Celsius.

4.3.2. Preparation of the substrates

In this work, sapphire substrate HEM (0001) $\pm$ 2 Deg., front side EPI polished, back side 50/80 was used. The sapphire substrates were cut into standard sizes of 7 x 5 mm side from a 50.8 mm Ø x 0.332 mm thick wafer. All substrates were ultrasonically cleaned in acetone, ACS 99.5% (CH_3COCH_3), for 15 min and then into ethanol 15 min, then were rinsed with deionized water and dried with gentle air pressure, then they were loaded into the deposition chamber.

4.3.3. The sputtering targets

Metallic copper and aluminum targets used were purchased from Superconductor Inc, USA. They were circular in shape with dimensions of 2″ diameter and 0.125″ thick, the purity of each of them was nominally 99.99%. Previous to deposition, targets were pre-sputtered during 10 min in order to remove any impurities from their surfaces.

4.3.4. Annealing setup

The diffusion controlled growth is due to heating at slow pace. In the present work, samples were heat treated using Rapid Thermal Annealing (RTA) in air. The advantage of using RTA process is that it partially restricts the diffusion but allows the film growth.

For this work, a 6" W x 6" D x 6" H Kerr 666 furnace was used. This furnace is capable of holding a sustained temperature of 1100°C and has a programmable 20 step heat ramp control.

Fig. 4.6 *Experimental Setup for Rapid Thermal Annealed used in this work.* (Dr. M. S. Tomar's Laboratory, UPR-M)

Working at full power, this furnace requires 2.5 h to reach its maximum temperature of 1100 °C and around for 20h for cooling down to 100 °C. These rates are not adequate for RTA.

However, the furnace described in the previous paragraph had an air vent on the top of it. In order to make RTA, this vertical hole was used as a channel to introduce and take out samples of it, assisted by an external device that provided faster temperature ramps. The external device consisted of mechanical arm made of alumina and driven by a stepper motor. A software code was written using Visual Basic Editor included in MS Excel 2007 for proper control of the speed. The experimental setup for Rapid Thermal Annealing employed in this work is shown in Fig. 4.6.

In order to obtain a constant temperature heating and cooling rate, a calibration curve (see Fig. 4.7) or the temperature at different vertical positions was made, and speed was adjusted accordingly.

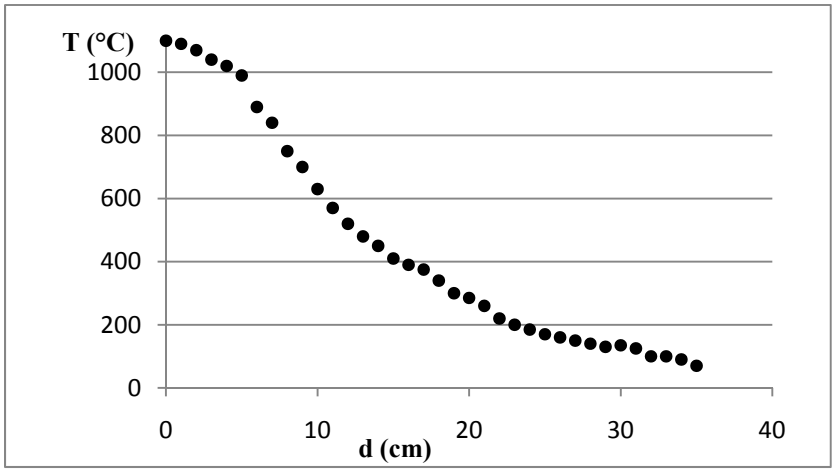

Fig. 4.7 *Calibration curve of Temperature vs. distance to the center of the furnace*

4.3.5. Sputtering Deposition Parameters

The many parameters involved in deposition of films by magnetron sputtering and the complex interrelations among all these parameters, requires them to be adjusted carefully in order to optimize of the quality of the films. For this work, the optimization of the deposition

parameters was based on the work of Shy et al. [41], then these parameters were adjusted to the specific necessities and the sputtering setup used in this work. The effect of changing the substrate to target distance, as well as the RF power was studied.

Substrate to target distances

For both cases the substrates were placed into the shutters to a distance of 4-6 cm from the target, in order to get the substrate parallel to the target and obtain uniformity in the thickness of the film. A scheme is shown in fig 4.8.

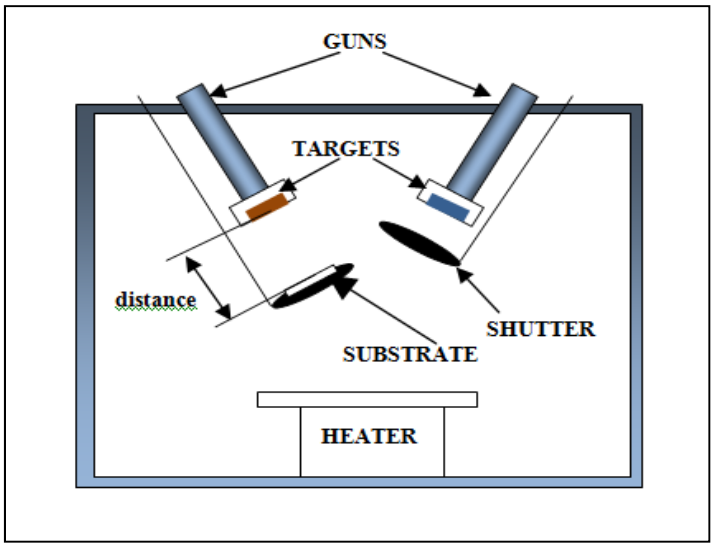

Fig. 4.8 *Schematic diagram of substrate to target distance*

The deposition parameters used for this work are presented in Table 4.1.

Table 4.1 *Deposition Parameters used for the present work*

Material	**CuO**	**Al_2O_3**
RF Power (W)	100W	150W
Deposition time (min)	30	30
Targets	Metallic Cu	Metallic Al
Substrate	Sapphire (0001)	Sapphire (0001)
Substrate temperature (°C)	Room temperature	Room temperature
Base Pressure (Torr)	$2.0x10^{-5}$	$2.0x10^{-5}$
Deposition Pressure	$1.0x10^{-2}$	$1.0x10^{-2}$
Sputtering Atmosphere	Ar +O_2	Ar +O_2
Substrate to target distance (cm)	4-6	4-6

5. Structural Characterization

5.1. X-rays Diffraction

In this chapter, a brief discussion is presented of the general principles of X-ray diffraction (XRD) for the case of single crystals and polycrystalline or "powder" samples, i.e. samples in which the sizes of the constituent crystals are very small (usually some few micrometers). In polycrystalline thin films, XRD characterization is usually carried out in order to verify the phase composition of the material, to analyze the size of crystallites and their preferred orientation, and to determine lattice deformations caused by residual stresses or structural defects.

X-rays are electromagnetic waves or radiation whose wavelength λ, is typically of the order of 1A˚ (10^{-10} m). This radiation is usually described by sine waves and characterized by their amplitude "$\boldsymbol{A}$" and their phase "$\boldsymbol{\varphi}$". The amplitude is related to the intensity "$\boldsymbol{I}$" of the wave, while the phase is the fraction of a complete cycle corresponding to an offset in the displacement from a specified reference point at time t = 0. When two o more waves are present, they could coincide in space and time and when this happen they are said to be "in phase", if not, they are said to have a ''phase shift'' δφ (measured in angular terms).

X-ray diffraction measurement is equivalent to measurement of the intensity of X-rays scattered from electrons bound to atoms. When many waves are present, the resulting amplitude is not just the sum of the individual amplitudes but depends on the phase shift, δφ and is given by:

$$I = \left[\sum_j A_j exp(i\varphi_j)\right]^2$$

After X-ray waves arrive to atoms at different positions, they become scattered and return to the detector with a relative phase shift that yields information about the relative atomic positions. Energy resulting from a single scattering event is very small, but if many scattering centers located at non-random distances from one another are present and if the wavelength is not modified after scattering (coherent scattering) constructive interference can occur giving rise to diffracted waves with higher intensities.

In order to obtain structural information of the material from X-rays diffraction, the Bragg analysis is generally followed, which describes the diffraction phenomena in terms of specular reflections of X-rays by sets of parallel planes. The incident angle can be varied to determine at which angles constructive interference, due to a phase offset, is obtained.

In the case of a crystal, a regular atomic pattern is present and lattices planes can be defined. Lattice planes act as mirror surfaces reflecting the incident radiation; they are defined by a set of integer indexes *hkl*, usually referred as Miller indices.

Fig. 5.1 shows two incident waves at parallel planes separated by a distance *d*. In general, when X-rays arrives the sample, they penetrate deep inside it and reflections at thousands of consecutive parallel planes take place.

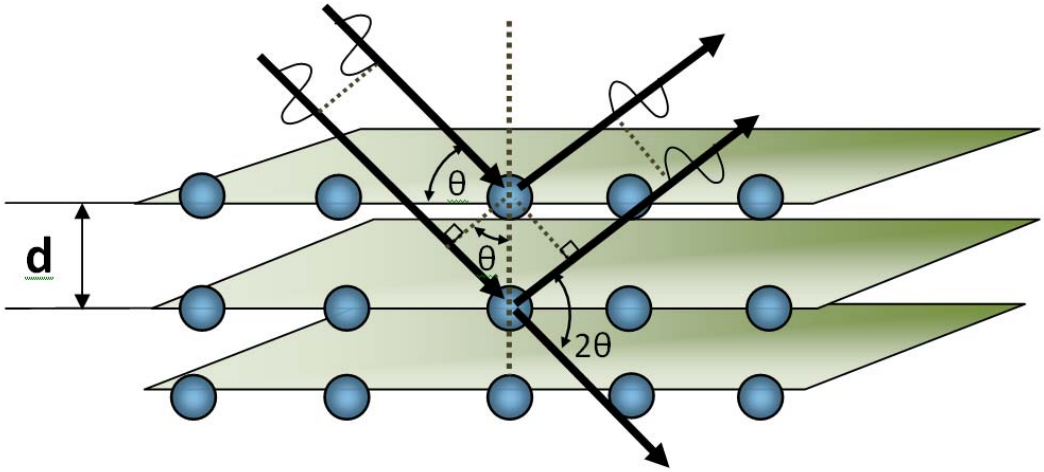

Fig. 5.1 *Geometry considered in Bragg analysis in which diffraction takes places at atoms in consecutive planes. Adapted from* [65].

Since all X-rays are reflected in the same direction, the scattered rays get superposed. It is evident from Fig. 5.1 that the second wave travels a longer distance Δ = PN + NQ. If Δ is an integer multiple of the wavelength, then constructive interference occurs:

$$\Delta = n\lambda, \qquad (n = 0, \pm 1, \pm 2, \ldots).$$

From fig 5.1 it can be shown that Δ= 2dsenθ, then the condition for constructive interference becomes:

$$n\lambda = 2d\sin\theta, \qquad (n = 0, \pm 1, \pm 2, \ldots).$$

This last equation is known as Bragg condition or Bragg Law. In crystalline solids, destructive interference completely destroys intensity in all directions except where Bragg Equation holds.

In polycrystalline samples the sizes and orientation of the constituent crystals (also known as crystallites) is not uniform and cannot be singled out to be characterized in the same way than single crystals. In a crystal, there are several families of planes with different orientations however interplanar distance among them is constant. In the case of a polycrystalline sample, the variable orientation and size of the crystallites will produce the number of families of planes contributing to one Bragg peak as well as the interplanar distances to be different than the single crystal case.

In polycrystalline diffraction it is preferable to have a sample with a smooth plane surface, with crystallites randomly distributed. Only crystallites having reflecting planes (*hkl*) parallel to the specimen surface will contribute to the reflected intensities.

In every XRD analysis for this work a Kristalloflex-Siemens, DACO-MP, power diffraction system with Cu-Kα x-ray tube (λ = 1.54056 Å) was used.

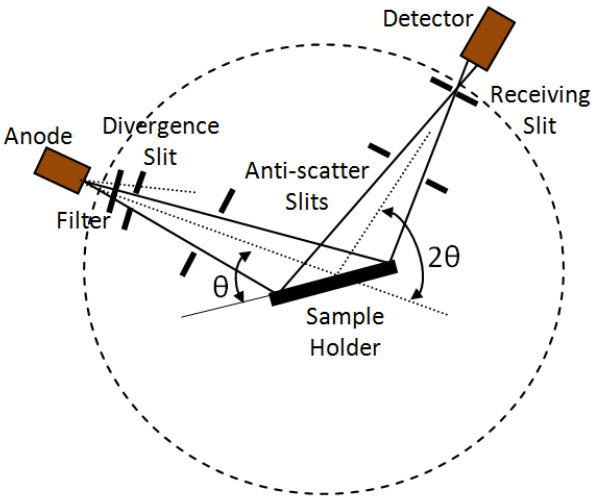

Fig. 5.2 *Schematic of the X-rays experimental setup*. Adapted from [65]

The x-ray scans were performed between 2θ values of 30° and 70° with a typical step size of about 0.02°. A schematic of the scanning setup is shown in fig.5.2. The X-ray source is located at the anode where X-rays beam is generated and after passing through some filters, divergence and anti-scatter slits reaches the sample, reflecting to finally reach the detector.

The diffraction files, or PDF chart files, used in this work for proper crystal structure identification were obtained from PDF II database of the International Center Diffraction Data (ICDD), formerly known as Joint Committee on Powder Diffraction Standards (JCPDS) and they are indicated correspondingly in following table:

Table 5.1 *PDF Files used for crystal structure assignment*

Compound	PDF File #
CuO	00-048-1548
Cu_2O	00-078-2076
$CuAlO_2$	00-035-1401
Al_2O_3	00-046-1212
$CuAl_2O_4$	00-078-1605

6. Electrical Characterization

Electrical characteristics of thin films are a function of the way they are grown. In particular, electrical properties of oxides are notably sensitive to the resulting degree of crystallinity, structural and electronic defect concentrations, void or porosity content, density, grain morphology, stoichiometry, etc. [66]. In order to get a better understanding of the underlying electrical mechanisms in the films, electrical resistivity, charier density and mobility are usually investigated.

6.1. Resistivity: Van der Pauw Method

The Van der Pauw method constitutes a very convenient way to measure the resistivity of a sample. Van der Pauw detailed how the specific resistivity of a flat arbitrarily shaped sample can be measured without knowing the current pattern, provided that: (1) the contacts are sufficiently small, (2) the contacts are on the periphery, (3) the lamellae is of uniform thickness and free of holes (singly connected). [67-68]

Although Van der Pauw method is applicable for samples of arbitrary shape, a common geometry has 4 electrical contacts at the four corners of a square or rectangular sample as shown in Fig. 6.1. A current is applied between two terminals, while the voltage is measured between the two opposite terminals.

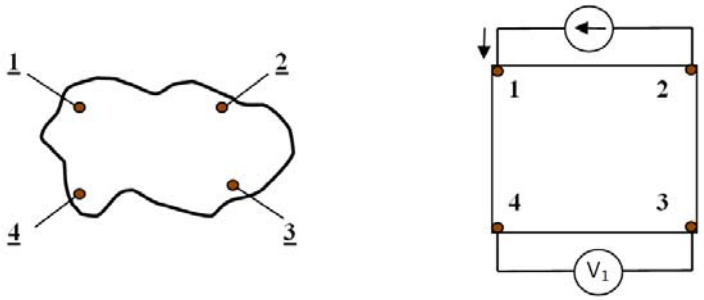

Fig. 6.1 *Geometries employed for Van de Pauw measurements.* Adapted from [69] and [71]

For a flat sample with contacts 1, 2, 3, and 4 along the periphery as shown in Fig. 6.1 and assuming that the conditions mentioned above are satisfied, the resistance $R_{12,34}$ according to Ohm's Law can be defined as: $$\mathbf{R_{12,34}} = \frac{\mathbf{V_3 - V_4}}{\mathbf{I_{12}}} = \frac{\mathbf{V_{34}}}{\mathbf{I_{12}}}$$

Where I_{12} represents the current that enters into the sample through contact 1, leaving through contact 2. Similarly, for $R_{23,41}$: $$R_{23,41} = \frac{V_4 - V_1}{I_{23}} = \frac{V_{41}}{I_{23}}$$

The configuration for these measurements taken with each possible terminal and current convention is shown in Fig 6.2,

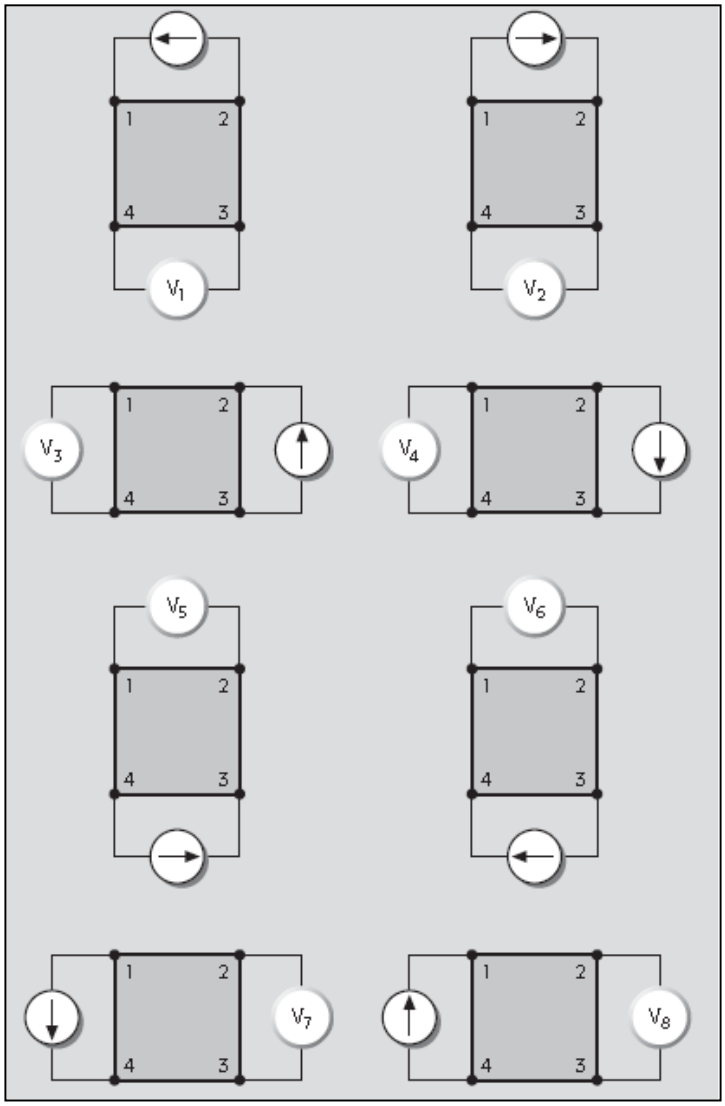

Fig. 6.2 *Standard configuration for Van der Pauw measurement* [69]

For testing repeatability and accuracy, the voltage and current's measure contacts are switched and measured again in both cases and switching of the polarities for each of the combinations mentioned is done in such a manner that we have two values of resistance R_1 and R_2 and a total of eight measurements:

$$R_1 = \frac{R_{12,34} + R_{34,12} + R_{21,43} + R_{43,21}}{4}$$

$$R_2 = \frac{R_{23,41} + R_{41,23} + R_{32,14} + R_{14,32}}{4}$$

According to van der Pauw, the resistivity can be calculated if the thickness of the sample, t_s, is known, by resolving:

$$\boldsymbol{e^{(-\frac{\pi t_s}{\rho}R_1)} + e^{(-\frac{\pi t_s}{\rho}R_2)} = 1}$$

We can calculate the average resistivity as:

$$\rho = \frac{\rho_1 + \rho_2}{2}$$

Where ρ_1 and ρ_2 are defined as follow:

$$\rho_1 = \frac{\pi}{\ln(2)} f t_s R_1 = \frac{\pi}{4\ln(2)} f t_s \left(\frac{V_{34}}{I_{12}} + \frac{V_{12}}{I_{34}} + \frac{V_{34}}{I_{21}} + \frac{V_{21}}{I_{34}}\right)$$

$$\rho_2 = \frac{\pi}{\ln(2)} f t_s R_2 = \frac{\pi}{4\ln(2)} f t_s \left(\frac{V_{41}}{I_{23}} + \frac{V_{23}}{I_{41}} + \frac{V_{41}}{I_{32}} + \frac{V_{32}}{I_{41}}\right)$$

In order to obtain the electrical conductivity, σ starting from the resistivity, the following relation was employed: $\sigma = 1/\rho$

The factor *f,* is a geometrical factor and depends mainly on the size and shape of the contacts, substrate dimensions, and thickness uniformity in the sample. The factor *f* is a function only of the ratio $R_r = R_1/R_2$, satisfying the relation:

$$\frac{R_r - 1}{R_r + 1} = \frac{f}{\ln(2)} arcosh\left(\frac{\exp\left(\frac{\ln(2)}{f}\right)}{2}\right)$$

This relation is plotted in Fig. 6.3. If f has low values, it means that the sample has too many geometric irregularities such as non-uniform thickness. For a symmetrical and uniform sample, f = 1; a value of at least 0.7 (or 10% of difference between calculated ρ_1 and ρ_2) is recommended as a criteria for thickness uniformity and reliability of measurement. [71]

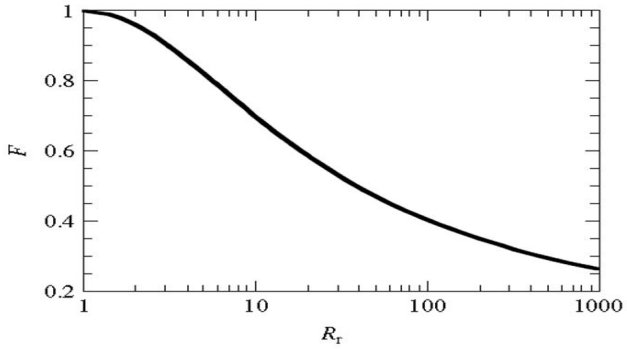

Fig. 6.3 *Plot of F vs.* R_r [71]

Assumption of negligibly small contacts located on the sample periphery is made in van der Pauw method, however real contacts have finite dimensions and may not be exactly on the periphery of the sample. When this is not the case, a correction factor C must be included.

In addition, it should be mentioned that corner contacts introduce less error than contacts placed in the center of the sample sides can be seen from Fig 6.4., where correction factor is plotted as a function of the ratio of contact size to sample side length d/l. If the contact length is less than about 10% of the side length, the correction is negligible for either contact placement [71]

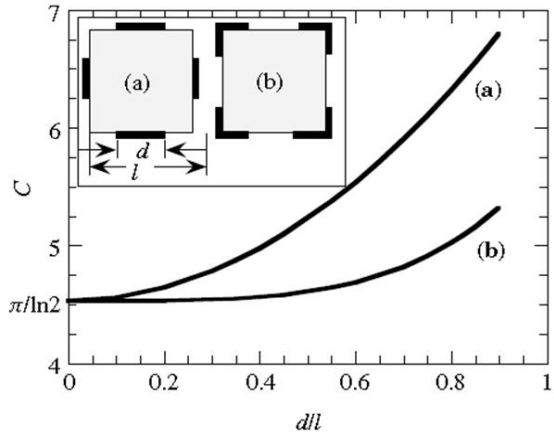

Fig. 6.4 *Influence of the electric contact on the correction factor* [71]

6.2. Hall Effect:

Hall Effect consists in the production of a voltage (Hall voltage) across an electrical conductor, resulting from the Lorentz force during the flow of an electric current in the presence of a magnetic field. The configuration for Hall measurements are such that a current is applied through two alternating terminals and voltage is measured across the diagonal of the sample. Eight such measurements are necessary. After voltage is measured, Hall coefficient R_H is obtained similar to the resistivity:

$$R_{H=}\frac{R_{H_1}+R_{H_2}}{2}$$

R_{H1} and R_{H2} are Hall coefficients in cm^3/C, defined as:

$$R_{H_1=}\frac{2.5\times10^7\, t_S\,(V_2-V_1+V_5-V_6)}{B\,I} \qquad R_{H_2=}\frac{2.5\times10^7\, t_S\,(V_4-V_3+V_7-V_8)}{B\,I}$$

where t_s is the thickness of the sample (in cm), B is the magnetic flux (in Gauss) and I is the measured current (in Amperes). According to the sign of the Hall coefficient, the type of conduction in the material could be established as p-type or n-type.

Also, Hall mobility $\boldsymbol{\mu}_H$, and charge carrier concentration p, can be estimated by employing the following relations: $\boldsymbol{\mu}_H = \frac{R_H}{\rho}$, $p = \frac{1}{q\,R_H}$ where ρ and q are the electrical resistivity and charge respectively.

The experimental setup used fot electrical characterization in this work is shown in fig. 6.5. It consisted of the following primary componentes 1) Keithley-224 D.C. Current source 2) A Keithley-6485 picoammeter 3) Keithley-2000 nanovoltmeter 4) Keithley-765 Switching mechanism 5) DIM-133 Magnetic Field sensor, 6) Helmoltz Coil Electromagnet with a maximum magnetic Field of 2T (teslas). All electrical contacts were made by using silver paint.

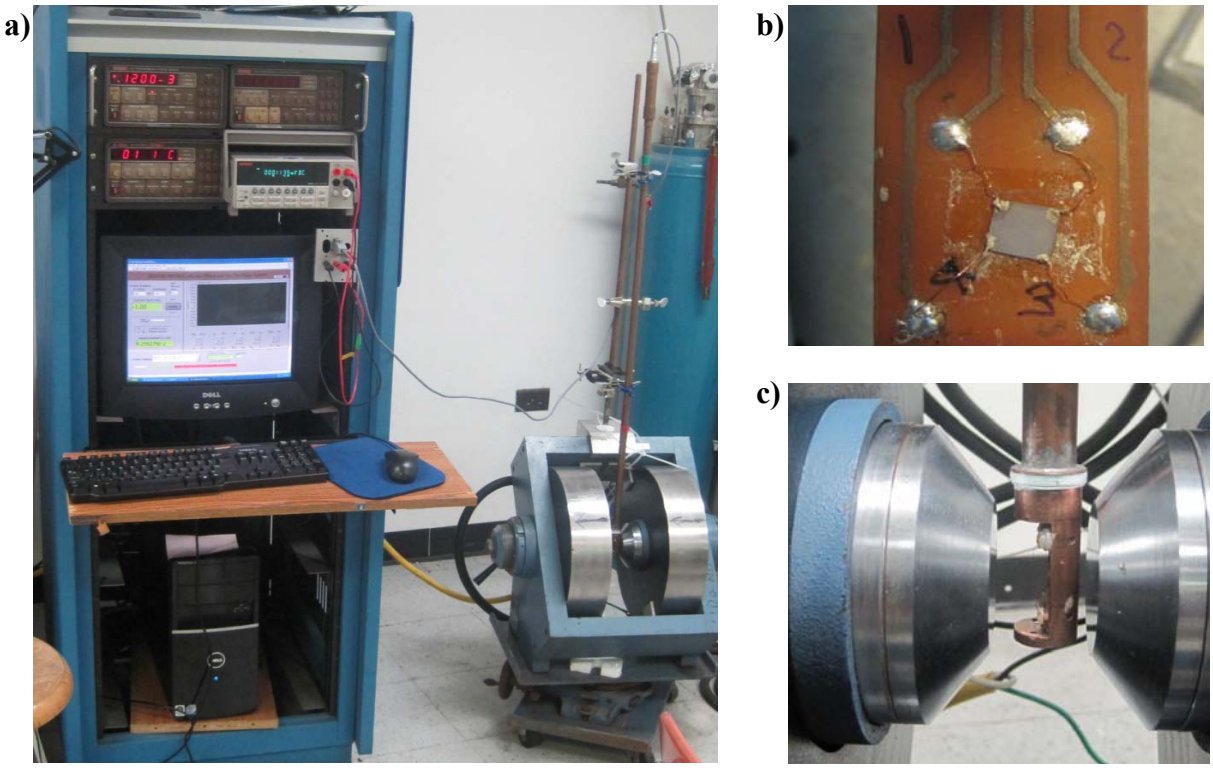

Fig. 6.5 *Experimental setup used fot electrical characterization* ***(a)****. Detail of the electrical contacts on the film for electrical measurements* ***(b)****. Detail of the sample properly placed at the center of the coils for measurements under influence of magnetic field* (Dr. R. Palai's Laboratory, UPR-RP)

Determination of film thickness: In order to proper calculation of electrical parameters of interest, thickness of the films had to be also measured. For this purpose a Tencor -100 Profilometer was used. The equipment used for this work shown in Fig 6.6. Each measurements was repeated 4 times and averaged in order to ensure accurate measurements. Complementary measurements of film thickness were also done with the aid of spectral reflectance technique.

Fig. 6.6 *Tencor-100 Profilometer Equipment used for this experiment* (Dr. F. Fernández's Lab., UPR-M)

7. Optical characterization

7.1. UV-Visible Spectrophotometry

UV-Vis measurements were carried out in order to study the optical transmittance and absorbance and calculating the band gap of $CuAlO_2$ thin films. For these measurements, a beam of light with a wavelength ranging within the visible and near ultraviolet regions is irradiated to a sample, and collected after passing through it, as shown in Fig. 7.1.

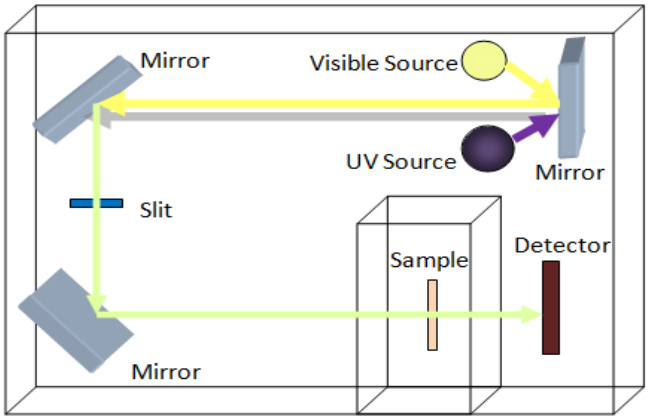

Fig. 7.1 *Schematic diagram of UV-visible optical measurements*

For the present work, a Beckman Coulter UV/Visible DU 800 Spectrophotometer, was used and it is shown in fig 7.2:

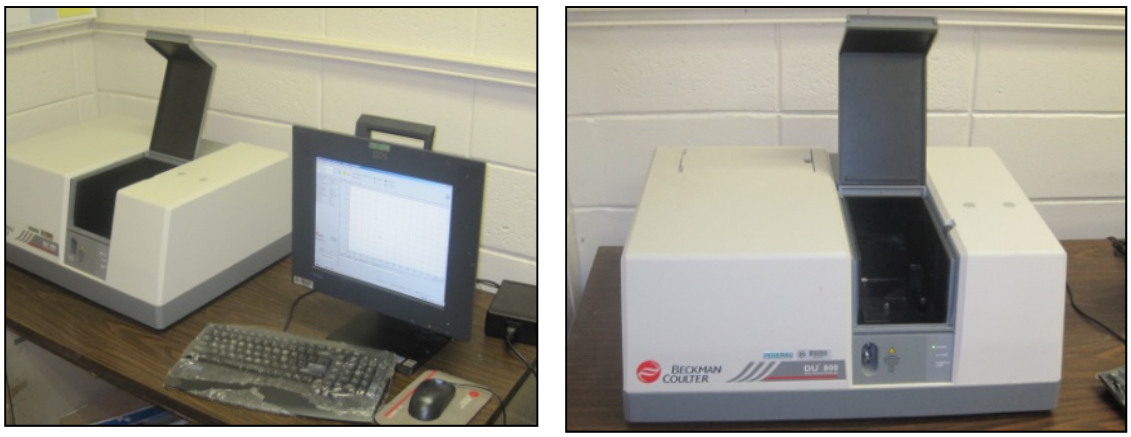

Fig. 7.2 *Beckman Coulter UV-Vis Spectrophotometer used for optical characterization (Dr. M.S. Tomar and O. J. Perales' Laboratory, UPR-M)*

Part of the incident radiation could be absorbed to the material. The absorbance in the visible region will determine the coloration or transparency of the samples. The optical absorption coefficient, α density is defined through the following equation:

$$I = I_o e^{(-\alpha d)}$$

where I is the intensity of the transmitted light, I_o is the incident light and d is the thickness of the film.

When incident light is absorbed by the material, it excites electrons from a low energy state to a higher energy state. These electronic transitions are usually categorized as direct or indirect transitions. If the bottom of the conduction band and the top of the valence band are placed at a common wave vector **k**, then it is called a direct transition; on the other hand, if they have different **k**-values, it is called an indirect transition. An indirect transition requires the intervention of a phonon in order to proper momentum conservation. These transitions are schematically shown in Fig. 7.3, where E_g represent the energy of the band gap. Vertical arrow represents the photon absorption process, while the wiggly arrow refers to the absorption or emission of a phonon.

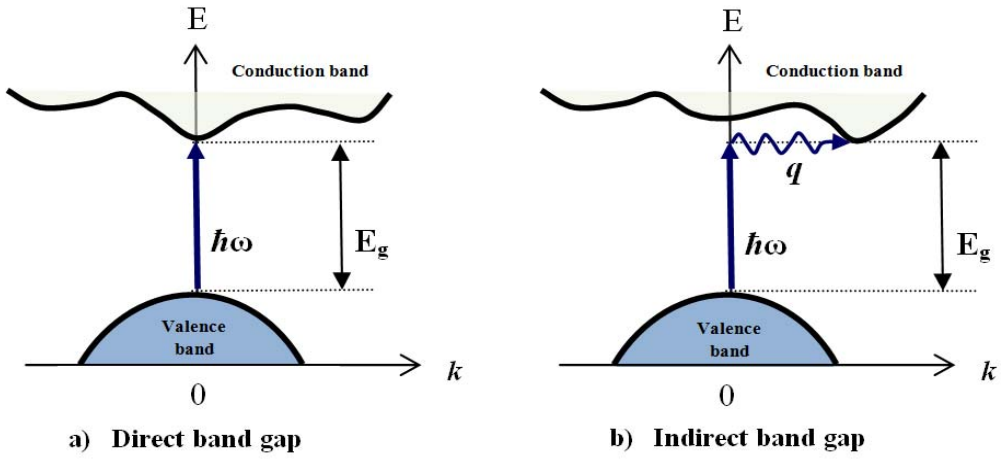

Fig. 7.3 (a) *Direct optical transition and* **(b)** *indirect optical transition between valence and conduction bands. The photon energy is ħω.* Adapted from [72]

The optical transmittance is related to the absorption coefficient through the relation:

$$T = \frac{I}{I_o} = 10^{-\alpha d}$$

In addition, knowing the absorption coefficient will also let us to calculate the energy band gap E_g of the material. In direct transition semiconductors, it can be shown [72] that for parabolic energy bands, the frequency dependence of the absorption coefficient α(ħω) is given by:

$$\left.\begin{cases} \alpha(\hbar\omega) = 0; & \hbar\omega < E_g \\ \alpha(\hbar\omega) \propto (\hbar\omega - E_g)^{\frac{1}{2}}; & \hbar\omega \geq E_g \end{cases}\right\}$$

When the energy of the incident radiation is lower than the energy band, there is no absorption; however, if a light beam of enough energy is directed to the sample, the absorption increases in a non-linear way as described by the formula mentioned above.

In the case of indirect semiconductors, due to energy conservation, absorption starts at an energy Eg - $\hbar\omega_{ph}$ below the band gap (where $\hbar\omega_{ph}$: energy of the phonon). It should be mentioned that indirect semiconductors also could have an optical transition between Γ valence- and conduction- band states; however this transition is at higher energies than the fundamental band gap [73].

In the range of the onset of the absorption edge, both the direct and indirect band gaps (E_g) can be determined by using the value of α in the following equation for semiconductors:

$$\alpha(h\nu)^{1/n} = \Lambda(h\nu - E_g)$$

where *h* is Planck constant, ν is the frequency of the incident photon, and Λ is a factor that does not depend of the frequency but on the effective masses. For direct semiconductors, n=1/2 while for indirect semiconductors n = 2.

III. Results and discussion

8. Structural characterization

8.1 CuO and Al_2O_3 deposition rates

In order to obtain $CuAlO_2$ thin films we first deposited the CuO films by RF sputtering from metallic copper target on sapphire (0001) substrates following the conditions described in Table 4.1. In an alternative approach we deposited CuO films on sapphire, and then one Al_2O_3 layer was deposited to have Al_2O_3/CuO/Sapphire system. To optimize uniformity of film thickness, target to substrate distance and deposition times were varied. Fig. 8.1 shows the dependence of film thickness on those parameters. RF Power was fixed at a value of 100W and reflected power was less than 10W. As-deposited films were dark gray in color, and thickness after deposition of 30 min was of 580 nm as measured with profilometer.

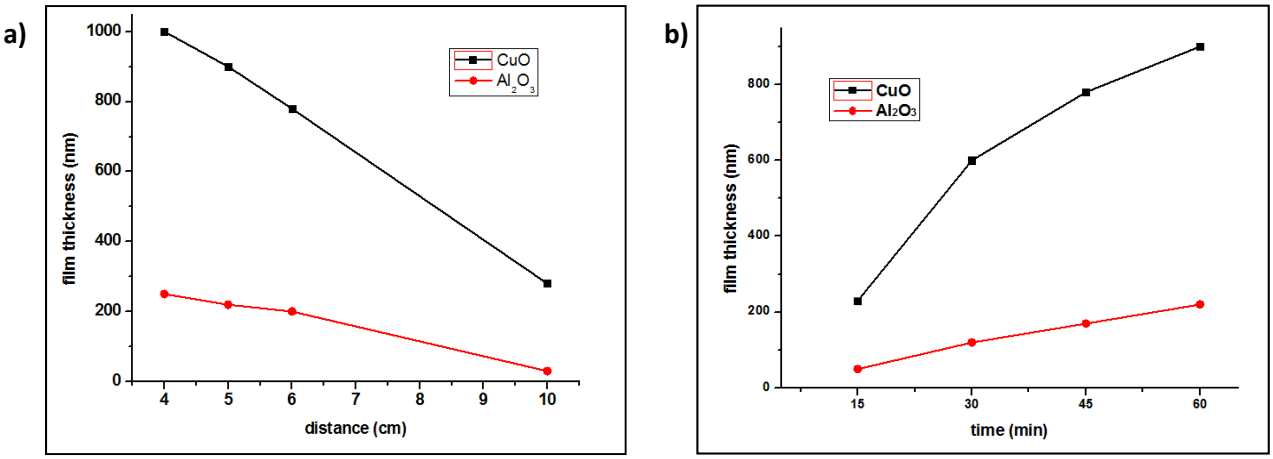

Fig. 8.1 *As-deposited film thickness dependence on **(a)** the target to substrate distance, films were deposited during 1 hour **(b)** the deposition time. RF power was 100W and 150W for the CuO and Al_2O_3 respectively*

It was found that for target to substrate distances below 5 cm, the thickness distribution of the film is not uniform, the center being thicker than the borders by approximately more than 15%;

however, films deposited at distance of 5 cm showed thickness variation lower than 6%. The as deposited CuO films were subjected to structural characterization using X- ray diffraction. The XRD patterns presented in Fig. 8.2 show the effect of substrate to target distance on the crystal structure. In the X-ray diffraction pattern for the three films deposited at distances of 4, 5 and 6 cm from the target, diffraction peaks at 2θ = 35.44◦ and 2θ = 38.85◦ corresponding to the (002) and (111) planes of CuO were observed, indicating the deposition of polycrystalline films.

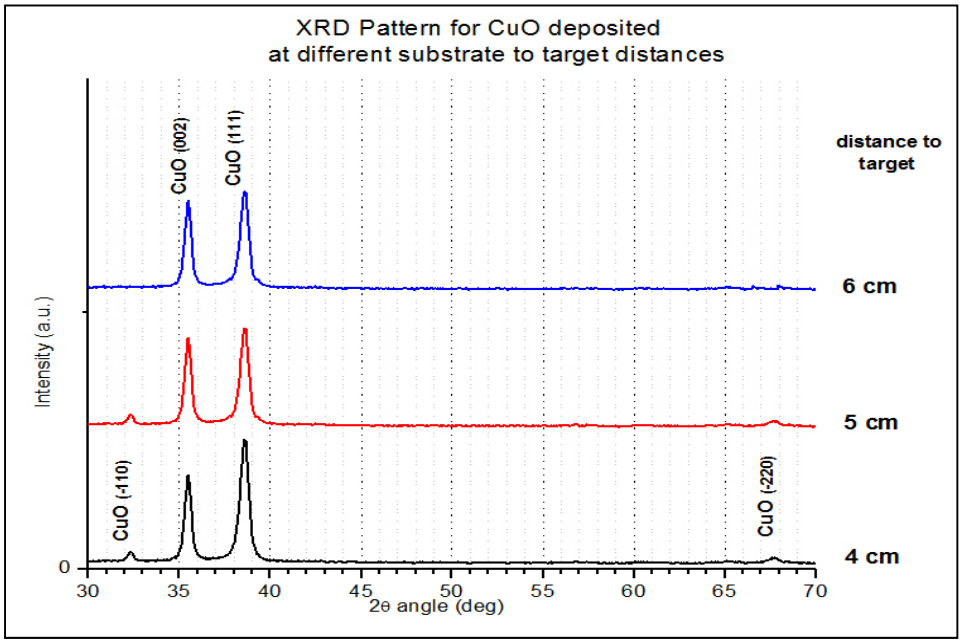

Fig. 8.2 *XRD Patterns for CuO film deposited during 30 min, at different substrate to target distances.*

As the distance was decreased higher polycrystallinity is observed and for samples deposited at distance of 5 and 4 cm to the target, as evident from the appearance of the (-110) and (-220) peaks at angles of 2θ = 32.52° and 67.76° respectively.

The observed results for the effect of deposition parameters (such as RF Power, substrate temperature and deposition pressure) on crystallinity and resulting phase, are in agreement the data reported by Chu et al. [74]. The effect of these parameters on the crystallinity of CuO in turn affects the phase formation of $CuAlO_2$ films.

8.2 $CuAlO_2$ phase formation after annealing process

The as synthesized CuO and CuO/Al_2O_3 films on sapphire substrate were subjected to rapid thermal annealing in air at 1100°C for 2 min, 10 min and 60 min in a 6"W x 6"D x 6"H Kerr 666 furnace. A comparison of the effect of annealing time on the crystalline structure for both films is presented and results of X-ray diffraction are shown in Figs. 8.3a-c.

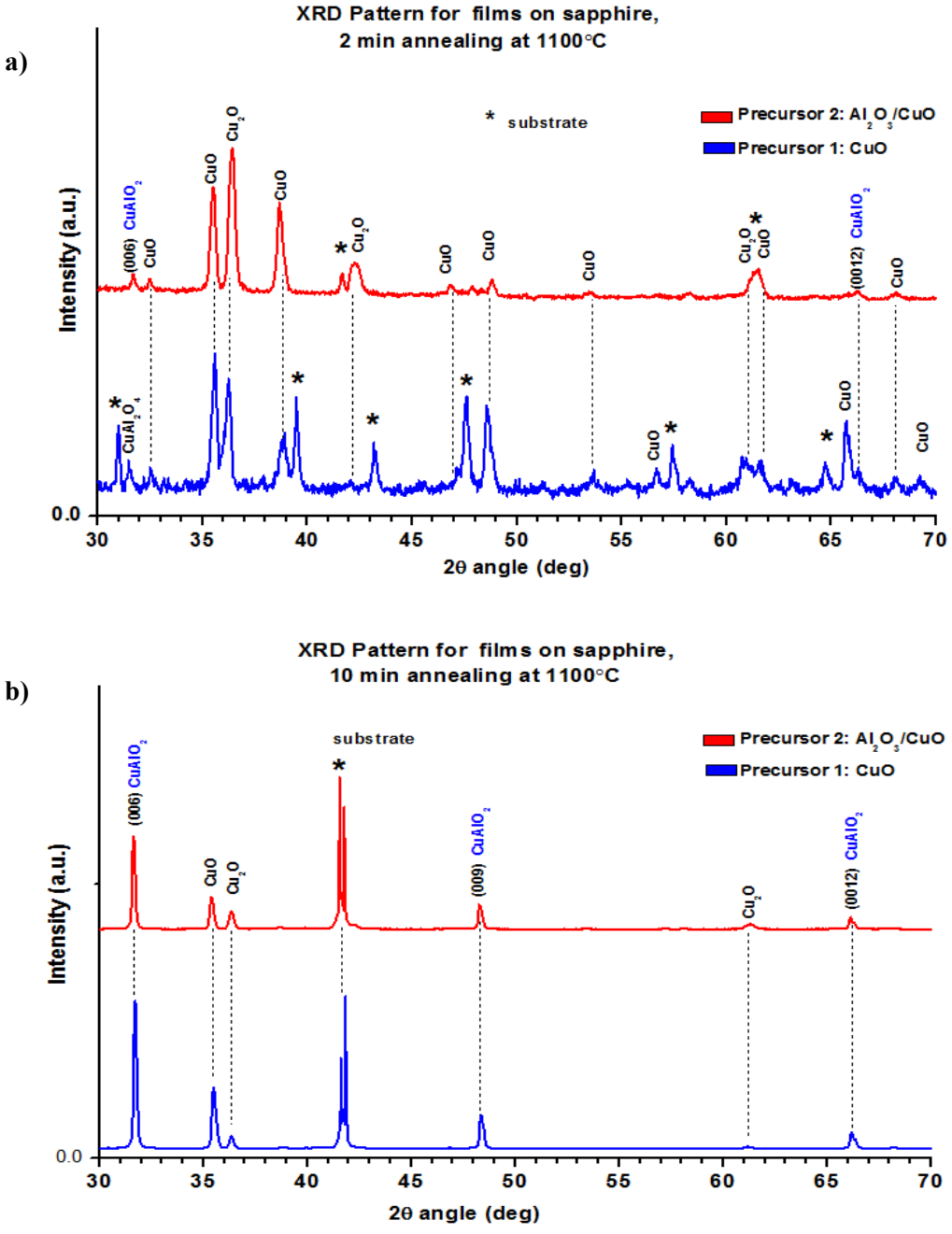

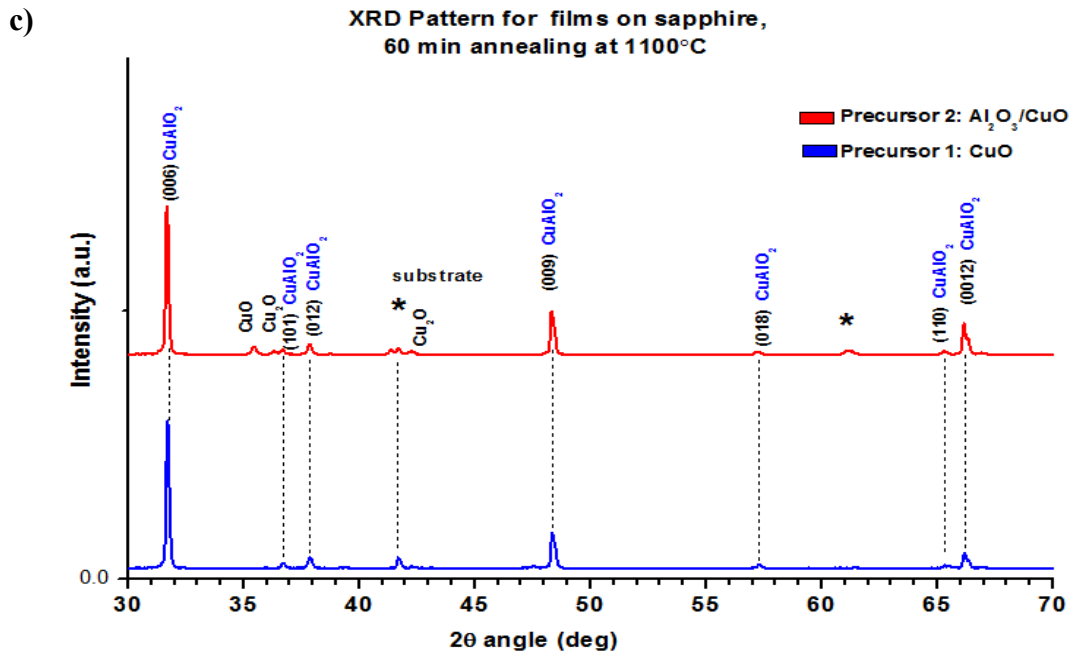

Fig.8.3 *XRD Patterns for films of CuO and Al_2O_3/CuO deposited on sapphire and annealed at 1100 °C during:* **a)** *2 min,* **b)** *10 min, and* **c)** *60 min.*

It can be seen that increasing the annealing time has favorable effect on formation of $CuAlO_2$ phase. Films annealed for 2 min (Fig. 8.3a), show many peaks belonging to CuO that were not present in the as-deposited film and are now present, because of higher crystallinity after annealing process. Films deposited from CuO on sapphire shows more peaks due to the substrate and a noisier pattern than the film deposited from Al_2O_3/CuO, which could suggest that after annealing for 2 minutes these films are thinner than the latter. There can also be observed some peaks belonging to Cu_2O, this would indicate that CuO gets reduced to Cu_2O changing its formal oxidation state from +2 to +1, as we have started from a phase pure CuO film. This is supported by the fact that after ten minutes of annealing (Fig. 8.3b), most of peaks corresponding to the CuO phase have disappeared and peaks related to $CuAlO_2$ phase now appears, where Cu has an oxidation state of +1.

After 10 min of annealing, the diffraction pattern for both films is very similar, a reduction of CuO and Cu_2O related diffraction planes at 2θ = 32.49°, 46.78°, 48.77°, 53.46° and 61.65° for CuO and 2θ = 32.49°, 46.78°, 48.77°, for Cu_2O when annealing time increased from 2 to 10 minutes is observed. For both films the relative intensities of the (002) peak of CuO at 2θ = 35.46° and (111) peak of Cu_2O at 2θ = 36.44° are reduced with respect to film annealed for 2 min, accompanied with increase in intensity of peak at 2θ = 32.49° corresponding to $CuAlO_2$, indicating that with time +2 state of copper changes to +1 oxidation state that favors the formation of $CuAlO_2$ as expected from phase diagram.

X-Rays diffraction patterns for films annealed during 60 minutes revealed the successful formation of $CuAlO_2$ phase as shown in Fig. 8.3 c. Diffraction peaks were identified using ICCD PDF Card # 035-1401 corresponding to $CuAlO_2$ with rhombohedral crystal structure and R-3m (group #166) space group symmetry. The high intensity of peaks (006), (009) and (0012) at positions 2θ = 31.68°, 48.37°, and 66.21° respectively, indicate preferred c-axis orientation of the films. However in films deposited from Al_2O_3/CuO, $CuAlO_2$ phase is not pure as the diffraction peaks related to CuO and Cu_2O are also present, suggesting that longer time is required for pure phase formation. In both cases, the presence of (101), (012), (018), (110), (006), (009) and (0012) diffraction planes suggests the formation of polycrystalline $CuAlO_2$ phase.

The aluminum necessary to react with copper oxide in order to get proper $CuAlO_2$ phase formation might be coming from the sapphire (Al_2O_3) substrate for films deposited from CuO. In the case of films deposited from Al_2O_3/CuO on sapphire, the top Al_2O_3 layer will also provide the required aluminum for the reaction. The reaction mechanism is believed similar to the described in the literature, and is shown in Fig. 8.4.

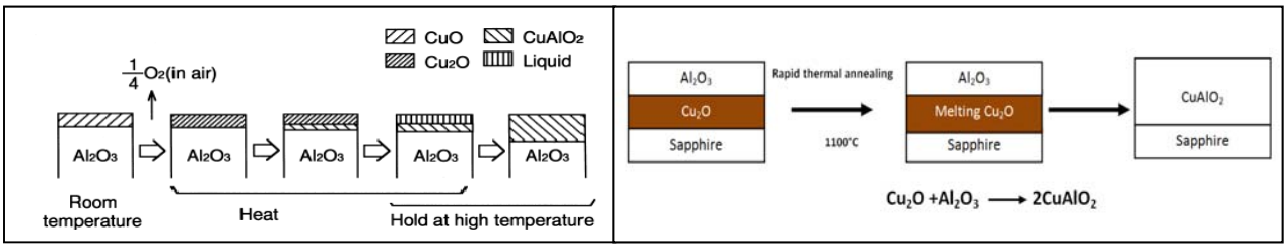

Fig. 8.4 *Scheme of the formation mechanism of CuAlO2 in films deposited from* **left)** *CuO on sapphire. Adapted from* [75], *and* **right)** *Al_2O_3/CuO on sapphire. Adapted from* [42]

Longer annealing periods were also explored. In the case of films deposited from CuO, exposition to annealing times of 2h and 3h respectively showed no additional diffraction peaks than the one exposed during one hour only. In the case of films deposited from Al_2O_3/CuO, growth of the $CuAlO_2$ upon further annealing times turns sluggish as inferred from the evolution of the relative intensities of peaks corresponding to $CuAlO_2$ versus those corresponding to CuO. For proper phase formation of $CuAlO_2$ films deposited as described, an annealing time of at least 300 minutes (5 hours) was necessary. X-Rays result for a sample annealed under the same conditions but during 5 hours revealed the formation of pure $CuAlO_2$ phase as can be seen in Fig. 8.5.b

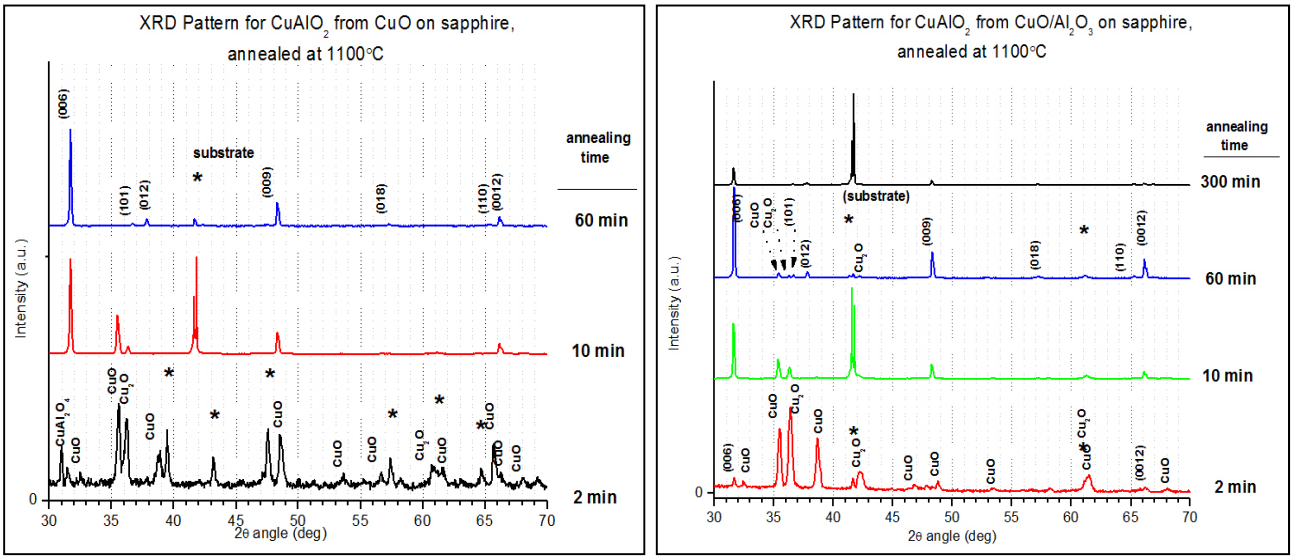

Fig.8.5 *XRD Patterns for films deposited from* **a)** *CuO on sapphire and* **b)** *Al_2O_3/CuO on sapphire and annealed at 1100 °C during different annealing times*

In addition, lattice parameters were calculated using X-Rays data for films annealed during 60 min. Hexagonal representation was used for rhombohedral primitive unit cell of $CuAlO_2$ (space group $R\bar{3}m$) as reported in the literature. From Bragg's diffraction Law, we have:

$$\frac{1}{d^2} = \frac{4\,(sin\theta)^2}{\lambda^2}$$

And for hexagonal crystal structure:

$$\frac{1}{d^2} = \frac{4}{3}\left(\frac{h^2 + hk + k^2}{a^2}\right) + \frac{l^2}{c^2}$$

From which, we obtain:

$$(sin\theta)^2 = \frac{\lambda^2}{4}\left[\frac{4}{3}\left(\frac{h^2 + hk + k^2}{a^2}\right) + \frac{l^2}{c^2}\right]$$

For calculating lattice parameter ***a***, peaks with values of l = 0 should be used. Replacing in the previous formula and solving for ***a***:

$$a = \frac{\lambda}{sin\theta}\sqrt{\frac{h^2 + hk + k^2}{3}}$$

For calculating lattice parameter ***c***, peaks with values h=k=0 are chosen, such that, after replacing and solving for ***c***, we will have:

$$c = \frac{\lambda l}{2sin\vartheta}$$

Cu-Kα wavelength of 1.541874 Å was employed corresponding to the X-Ray diffraction equipment used for this work. Peak 110 (l =0), at 2θ = 65.32° was chosen for calculation of lattice parameter ***a***, while for lattice parameter ***c***, (006) and (009) peaks were used, (angular position 2θ = 31.71° and 48.34° respectively), and average value was taken. Calculated lattice parameters were ***a*** = 2.8572 Å and ***c*** = 16.9384 Å. It is noteworthy the close agreement with the values reported in the literature: are: ***a*** = 2.858 Å, ***c*** =16.958 Å. [5]

Profile fitting, angular position and FWHM estimation for $CuAlO_2$ film was done with the aid of computer software MATCH! 1.5. Peak data are taken as parameters in a constrained least-squares refinement. Fig. 8.6 shows characteristics results obtained with the software for $CuAlO_2$ film deposited from CuO on sapphire. Most of the peaks shown correspond to the desired material $CuAlO_2$, and there are also present some peaks corresponding to the substrate (2θ =41.68° and 47.61°). The right column compares the calculated values with those of the database values corresponding to $CuAlO_2$ (PDF chart # 35-1401).

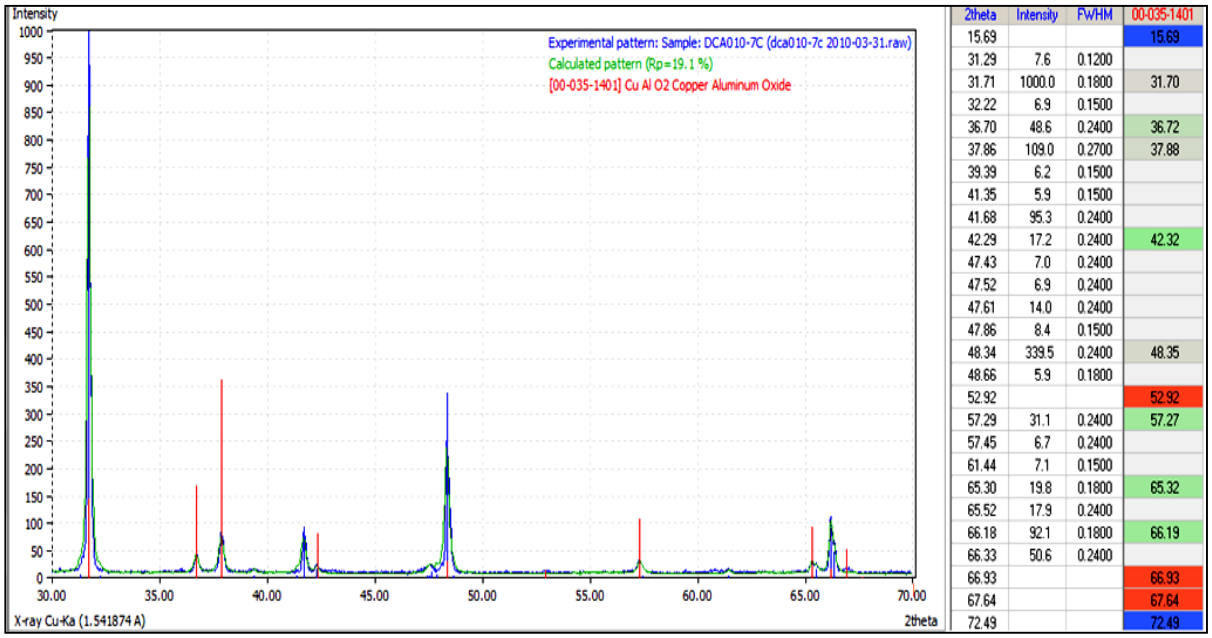

2theta	Intensity	FWHM	00-035-1401
15.69			15.69
31.29	7.6	0.1200	
31.71	1000.0	0.1800	31.70
32.22	6.9	0.1500	
36.70	48.6	0.2400	36.72
37.86	109.0	0.2700	37.88
39.39	6.2	0.1500	
41.35	5.9	0.1500	
41.68	95.3	0.2400	
42.29	17.2	0.2400	42.32
47.43	7.0	0.2400	
47.52	6.9	0.2400	
47.61	14.0	0.2400	
47.86	8.4	0.1500	
48.34	339.5	0.2400	48.35
48.66	5.9	0.1800	
52.92			52.92
57.29	31.1	0.2400	57.27
57.45	6.7	0.2400	
61.44	7.1	0.1500	
65.30	19.8	0.1800	65.32
65.52	17.9	0.2400	
66.18	92.1	0.1800	66.19
66.33	50.6	0.2400	
66.93			66.93
67.64			67.64
72.49			72.49

Fig. 8.6 *XRD profile fitting and estimated values obtained with the aid of computer software MATCH! 1.5c, for $CuAlO_2$ film deposited from CuO on sapphire.*

Annealing conditions affect the quality and physical properties of the films. Optical and scanning electron microscopy techniques were used for inspecting the surface morphology of films. Fig. 8.6 shows scanning electron micrographs of CuO films on sapphire (Al_2O_3) before

and after annealing. It can be observed that as-deposited film is has a very uniform size distribution and crystallite size is approximately about 0.2 μm, however after rapid annealing on air, during 2 min at 1100 °C, the crystallite sizes increase to about 0 .35 μm and some aggregates start forming. In addition, it can be observed that the surface morphology is not flat anymore and will change depending on the specific processing conditions.

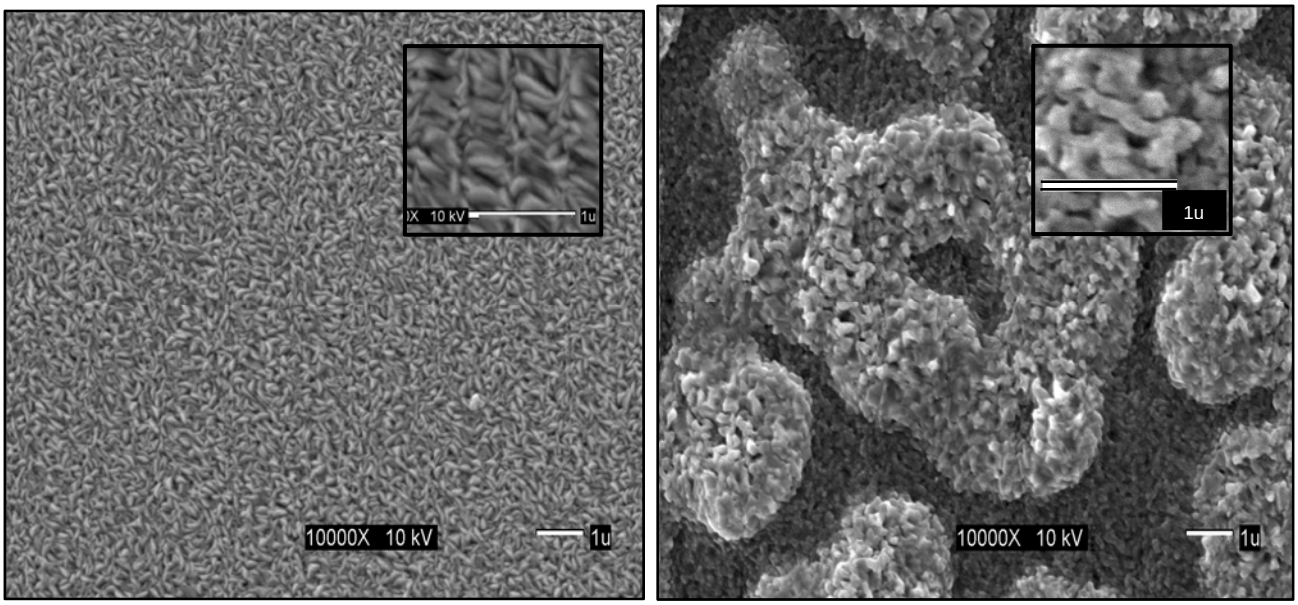

Fig. 8.7 *Scanning electron micrographs of CuO films on sapphire (Al_2O_3).* **Left:** *as-deposited film.* **Right**: *film after 2 min. of rapid annealing on air, at a temperature of 1100 °C.*

In the case of films deposited from Al_2O_3/CuO films, perversely to previous approach the recrystallization process primarily dictate the phase formation instead of diffusion process, as is suggested from optical micrographs shown in Fig. 8.7. The increasing annealing time could induce the formation of new grain boundaries and reduction in grain size suggesting that recrystallization have more prominent effect on phase formation. Moreover, change in color of grains also indicates the diffusion process is slow in this case compared to diffusion of CuO in oriented Al_2O_3.

a) 2 *min annealing*

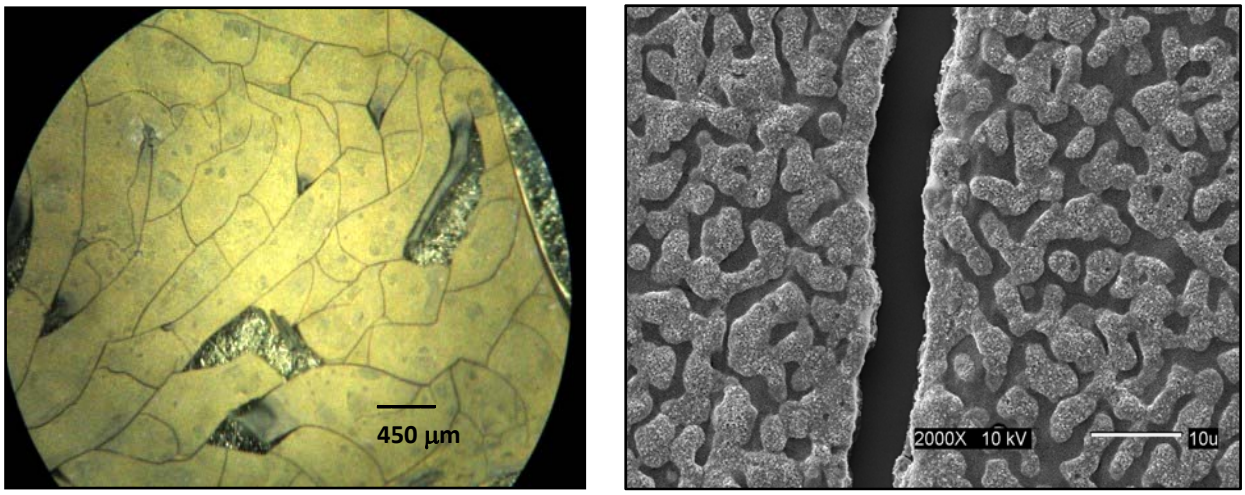

b) 10 *min annealing*

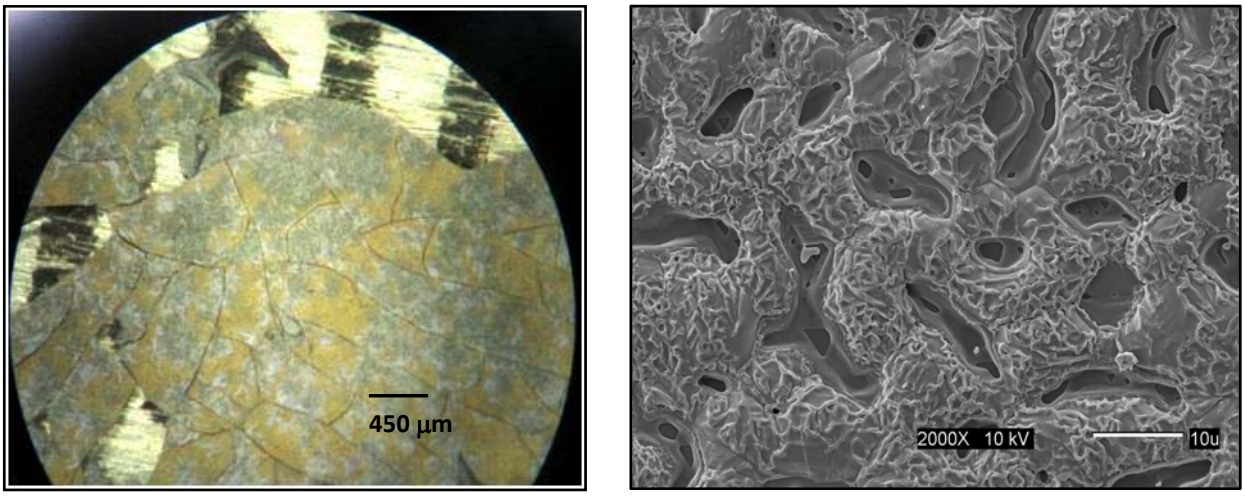

c) 60 *min annealing*

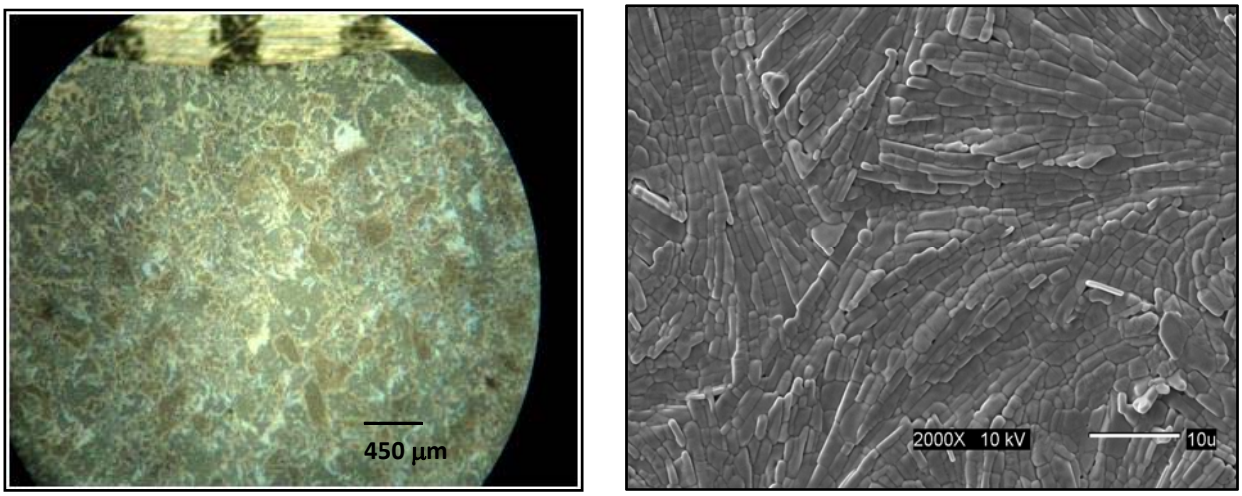

Fig. 8.8 *Recrystallization behavior of films annealed to 1100° C, with different annealing times*

Optical microscope was used also to track the evolution of optical transparency with increasing annealing time. Fig. 8.8 shows optical micrographs for films deposited from CuO. Films annealed during 2 minutes are opaque in the visible region and grayish in color. It is evident that films annealed during longer periods present higher transparency.

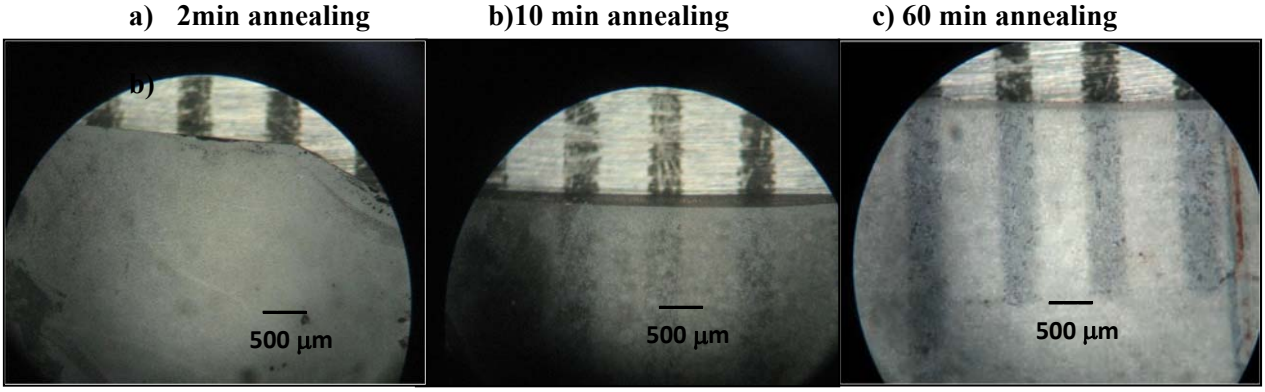

Fig. 8.9 *Optical Microscope photograph of CuO films on sapphire after* ***a)****2 min,* ***b)****10 min and* ***c)****60 min of annealing at 1100°C.*

Longer annealing periods were also explored, a very slight improvement of optical transparency was observed. However, this might be related to the fact that thickness of the films decrease with annealing time as shown in Fig. 8.9.

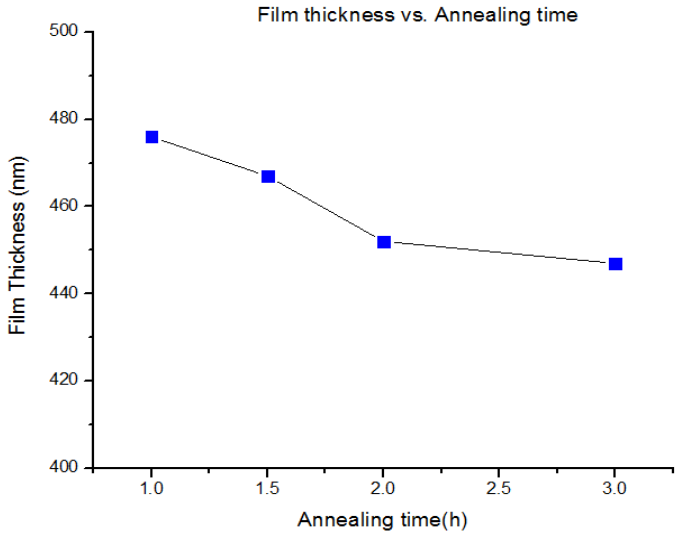

Fig. 8.10.*Variation of the film thickness with the annealing time.*

In addition, a longer exposure to thermal treatment would provide the required energy for atoms to diffuse across the material and properly accommodate into the lattice, leading to a higher crystallinity and hence an increment in optical transparency.

For films deposited from Al_2O_3/CuO, longer annealing times and slower cooling rates were also explored. It could be seen from Fig. 8.10 that the faster cooling rates results in the formation of larger grains along with the formation of voids. The films with slower cooling rate of 0.1 C/s reveals the uniform films surface apparently with no grains and voids.

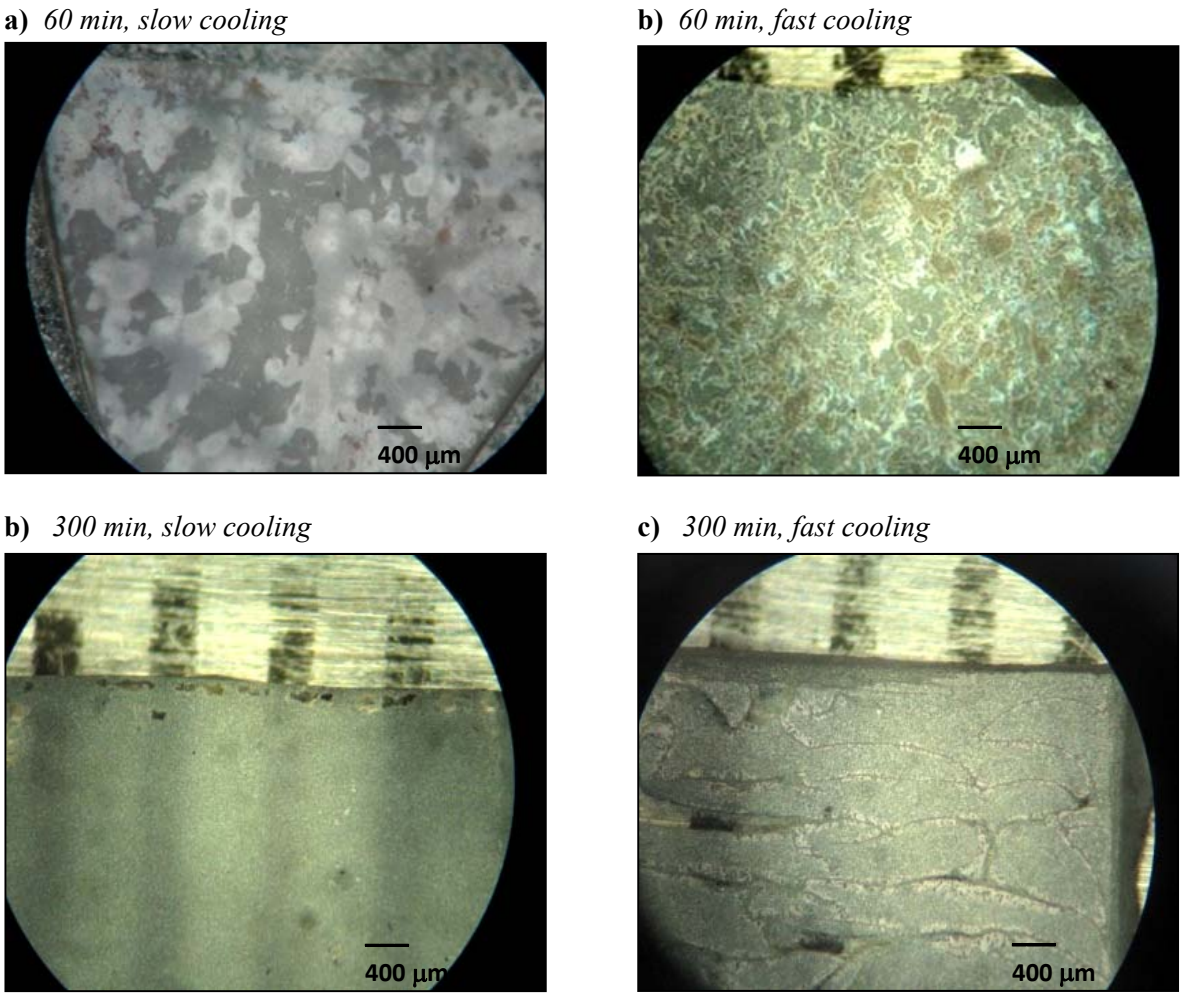

Fig 8.11. *Surface evolution under different annealing and cooling conditions. Fast cooling: 10 °C/s, slow cooling: 0.1° C/s*

9. Optical Measurements

Transparency is one of the key parameters for transparent conductor thin films. They are expected to be colorless. In this work, $CuAlO_2$ films were obtained by annealing samples of CuO and CuO/Al_2O_3 on sapphire, separately. After cooling, the samples coming from CuO were moderately transparent, while most of the samples coming from Cu/Al_2O_3 were light gray in color. Fig 9.1 shows the optical transmittance spectra for $CuAlO_2$ thin films obtained from annealing CuO and from CuO/Al_2O_3 measured with a UV-visible spectrophotometer. Transmittance of the film prepared by annealing of CuO film was almost 60%, this is approximately two times more transparent than the one obtained by annealing CuO/Al_2O_3 film; however is not as high as that for n-type TCOs (above 80%).

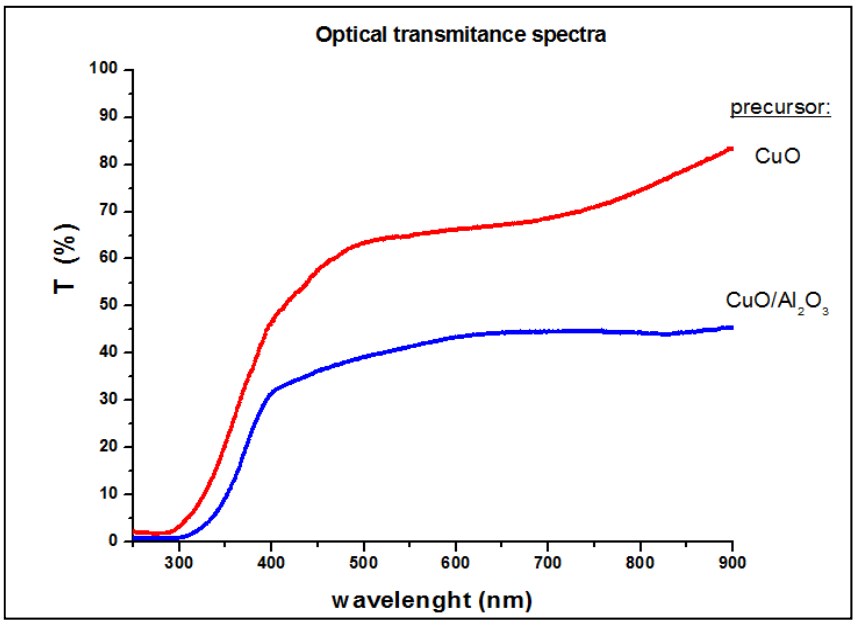

Fig.9.1 *Optical Transmittance of $CuAlO_2$ prepared from two different precursors*

The main factors that affect transparency of the films are surface roughness, defects and coloration. Surface roughness will decrease the transmittance because of scattering of the

incident light into the film. Coloration is another factor to consider; most of the samples prepared by annealing Al_2O_3/CuO revealed a grayish coloration. It is possible that during the annealing process, additional oxygen atoms become inserted into the delafossite structure occupying sites between the Cu atoms in the Cu planes promoting Cu-O-Cu- linkages. In that case, according to Wager [76], Cu(I) atoms would become locally oxidized during the initial stages of this O insertion process, promoting the apparition of isolated Cu(II) atoms and an intense coloration of the samples. In addition, Buljan [77] suggests that coloration in $CuAlO_2$ is due to d^{10} - d^{10} weak homoatomic interactions between copper ions.

Thickness of the films could also play a role in the increment of transmittance. In order to investigate this effect, evolution of film thickness and optical transmittance during annealing process were plotted and are shown in Fig. 9.2. It can be seen that thickness decreases correlated to an increase of optical transmittance for longer annealing times; however the overall change in thickness is less than 10%, leading to the hypothesis that although thickness diminution could be improving optical transmittance, it is not the main factor.

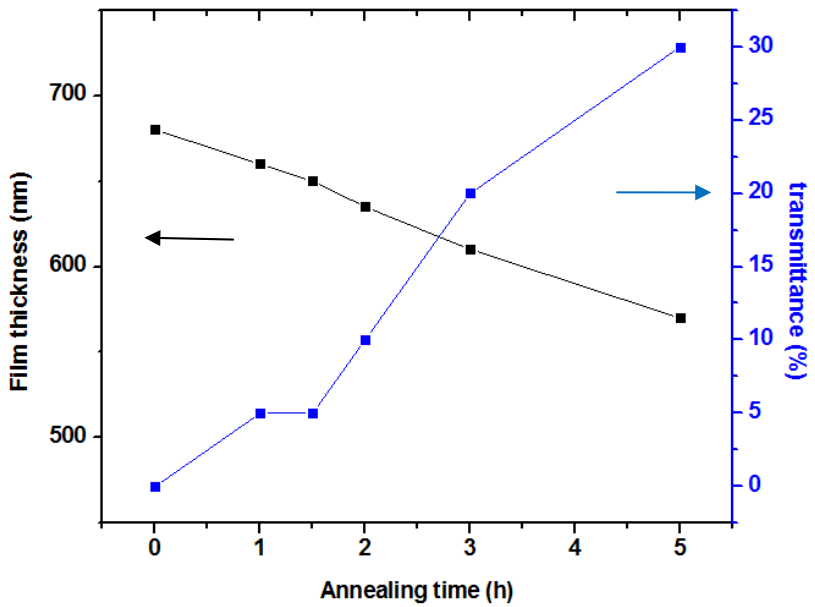

Fig. 9.2. *Film thickness and optical transmittance dependence on annealing time. Cooling rate: 0.1 °C/s*

In order to determine the different transitions and optical band gaps E_g of the material, the frequency dependence of the absorption coefficient α, was used:

$$(\alpha h\nu)^{1/n} = \Lambda(h\nu - E_g)$$

where the exponent n depends on the type of transition: n = 2 for indirect allowed transitions and n = ½ for direct allowed transitions. The Λ factor also depends on the type of transition. The experimental absorption spectra were conveniently plotted in Tauc diagrams [78], in which the value of $(\alpha h\nu)^{1/n}$ is taken as the ordinate and the energy hν, as the abscissa. The resulting plot have a linear region that, according to the equation above mentioned, when extrapolated to the energy intercept on the α = 0 axis, the interception point yields the value of the energy gap.

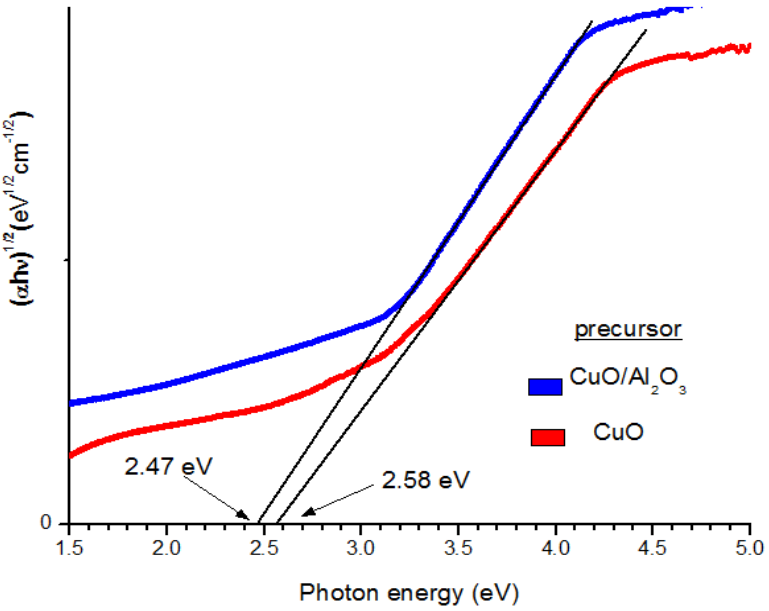

Fig.9.3 *Estimation of Indirect Energy gap for $CuAlO_2$ films*

It was found (see Fig. 9.3) that for $CuAlO_2$ films prepared from CuO/sapphire, the indirect band gap was 2.58 eV, while sample for prepared from Al_2O_3/CuO/sapphire a value of 2.47 eV was obtained. The region selected for linear fits were those with the lowest mean quadratic error (MSE). These values are in agreement with other results on thin films reported in

the literature [17],[19]. The obtained results are lower than the reported values for indirect gap on single crystals suggesting influence of strain effects.

The direct allowed optical band gaps for $CuAlO_2$ thin films were also found by evaluating the linear region of the absorption edge in Tauc plots, where $(\alpha h\nu)^2$ vs. $h\nu$ is plotted and shown in fig 9.4. Direct band gaps were 3.72 and 3.54 eV, for the $CuAlO_2$ films obtained from CuO and CuO/Al_2O_3 precursors respectively.

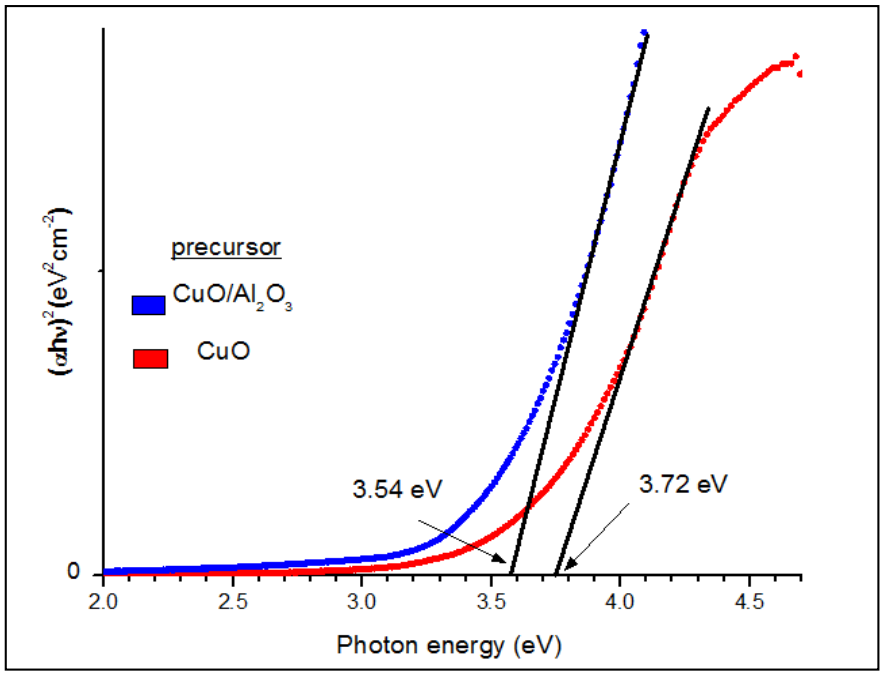

Fig.9.4 *Tauc Plot for estimation of Direct Energy gap of $CuAlO_2$ films*

The difference between these two values could probably be attributed to the synthesis process. The Cu/Al ratio content is reported to produce a blue shift [40] of the optical band gap which could be the most probable reason in our samples, and characterization of the chemical composition would help to clear this point.

10. Electrical Measurements

Other key property of transparent conductors is electrical conductivity. It is desirable to have high electrical conductivity, at least comparable to n-type transparent conductors. Reported electrical conductivity for $CuAlO_2$ thin films is of the order of $\sigma \sim 10^{-1}$ -10^{-2} $S.cm^{-1}$. Recently, Dong [20] have reported values of conductivity as high as 10^2 Scm^{-1}, however to the present time these results have not been reproduced by others.

In this work, the resistivity of the $CuAlO_2$ films prepared by two different approaches as mentioned in previous chapters was measured by using the van der Pauw technique. Electrical contacts consisted of copper wires soldered on the four corners of each film by using silver paint. Films made by annealing of CuO on sapphire showed lowest resistivity (9.91 Ω-cm). Figs. 10.1 (a) and (b) show the variation of resistivity with annealing conditions, namely annealing time and cooling rate for $CuAlO_2$ films made from CuO precursor.

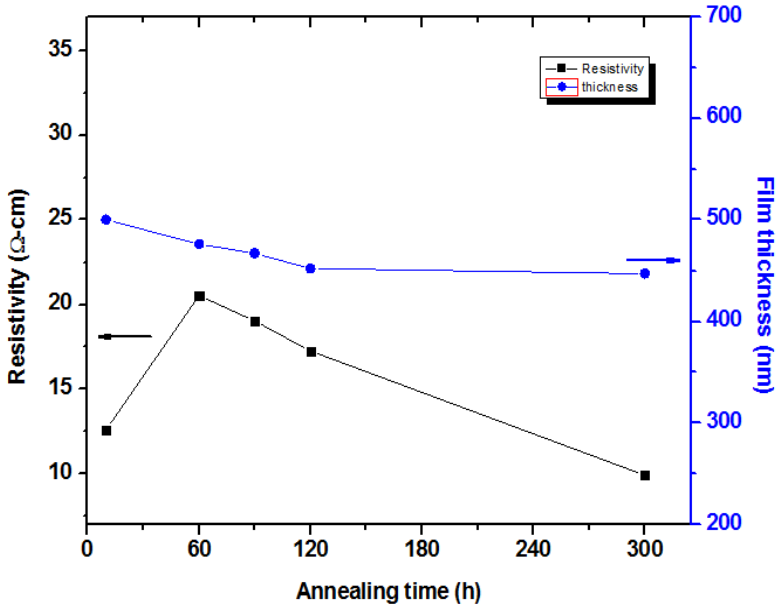

Fig. 10.1 (a) *Variation of resistivity with annealing time. Cooling rate was fixed at 0.1 °C/s*

It can be seen (see Fig. 10.1a) that longer annealing led to a linear decrease of resistivity. Although sample annealed during 10 min showed low resistivity, from X ray diffraction (Fig. 8.5) it can be noted the presence of CuO phase, which contributes to lower the resistivity of the film. Resistivity increase seems to be correlated with increase in film thickness (see Fig. 10.1a), suggesting the appearance of lattice defects in thicker films hindering the charge carriers transport across the sample, and hence leading to an additional percentage of resistivity, however this behavior is contrary to the expected for thin films, given that lattice defects such as vacancies, interstitials and dislocations are usually more abundant through the first stages of the film growth. Banerjee et al. [15] found a like trend for $CuAlO_2$ films deposited by DC sputtering, and attributed the increase of conductivity to excess of oxygen atoms incorporated during the annealing process, though the diffusion process of oxygen still remains unclear. Moreover; simultaneous to phase formation and crystallization process favored with longer annealing times, evaporation process could take place leading to substantive material loss and then to a reduction in film thickness. This is supported by the results obtained from XRD analysis shown in Fig. 8.5.

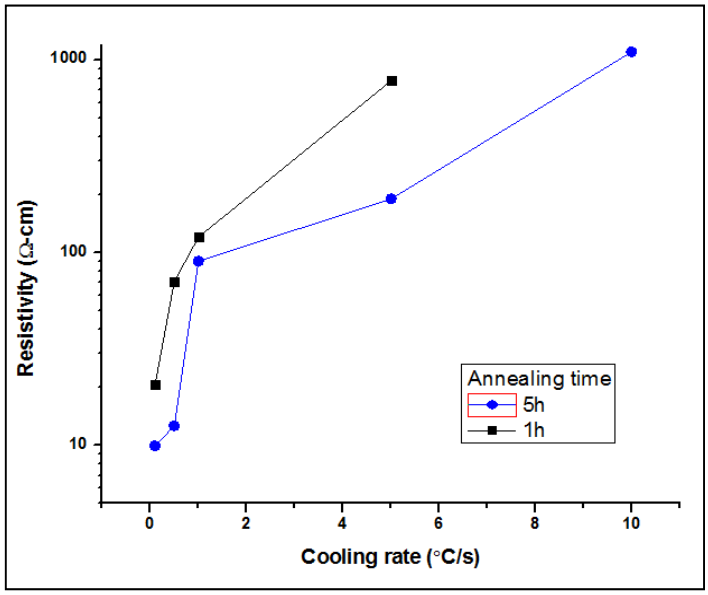

Fig. 10.1 (b) *Variation of resistivity with cooling rate. Film annealed during 1h with a cooling rate of 10 °C/s was too resistive for measurement.*

Resistivity increased with faster cooling rates, as shown Fig. 10.1 b. This could be related to the fact that when samples were cooled too fast, without enough time to reach thermal equilibrium, cracking and/or peeling of the film surface was the unavoidably result (thermal expansion coefficient along the a axis are 8 and 12 x 10^{-6} K^{-1}, while along the c axis are 9 and 6x10^{-6} K^{-1} for α-Al_2O_3 and $CuAlO_2$ respectively). Even in the cases where cracking was not visible to naked eye, SEM characterization revealed microscopic fissures of the films (see Fig. 10.2 below). Also, it is remarkable that films annealed during 5 hours showed lower resistivity than those annealed during 1h, independently of the cooling rate.

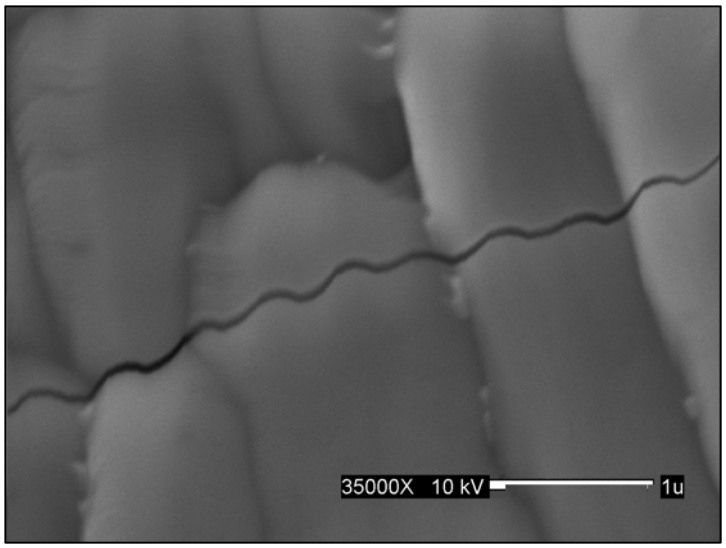

Fig.10.2 *SEM photograph of $CuAlO_2$ film showing cracking of the film not visible to naked eye. Cooling rate was 1 °C/s.*

$CuAlO_2$ films prepared by annealing Al_2O_3/CuO on sapphire showed higher values for resistivity than films prepared from CuO on sapphire, however the same trends described in the previous paragraph were found. Table 10.1 shows some of the main electrical properties measured for the films prepared from these two different precursors. Electrical parameters were calculated as described in chapter 6. For all of the samples slow cooling (0.1 °C/s) was used in order to get better surface quality of the films.

Besides, conductivity increase for longer annealing time, could be associated with diffusion time required to complete reaction of the precursor film with the substrate. The highest value for conductivity was 1.01 $x10^{-1}$ S cm^{-1} and the sample corresponds to the diffusion of CuO in sapphire substrate using rapid thermal annealing for 5h. This value is comparable to reported in the literature. The sample prepared from CuO/Al_2O_3, was too resistive for electrical measurements.

Table 10.1 *Measured electrical properties for $CuAlO_2$ films annealed at slow rate* (0.1 °C/s)

Precursor	Annealing time (h)	Resistivity (Ω-cm)	Conductivity (S cm-1)	Hall coefficient (cm^3C^{-1})	Hall mobility (cm^3C^{-1})	Carrier concentration (cm^{-3})
CuO	1.0	20.54	$4.87 x10^{-2}$	+1.72	$8.37x10^{-2}$	$3.63x10^{18}$
CuO	2.0	17.26	$5.79 x10^{-2}$	+1.85	$1.07x10^{-1}$	$3.37x10^{18}$
CuO	5.0	9.91	$1.01x10^{-1}$	+2.64	$2.66 x10^{-1}$	$2.36x10^{18}$
Al_2O_3/CuO	1.0	$>10^8$	-	-	-	-
Al_2O_3/CuO	2.0	530	$1.89x10^{-3}$	+7.5	$1.42x10^{-2}$	$8.32x10^{17}$
Al_2O_3/CuO	5.0	138	$7.25x10^{-3}$	+6.95	$5.04x10^{-2}$	$8.98x10^{17}$

Positive sign of Hall coefficient indicates p-type conductivity. Films deposited from CuO/sapphire showed an increment in electrical conductivity and Hall mobility with longer annealing times, this increment could be associated with the increase of grain size and hence improvement of the grain boundary, minimizing the scattering or trapping of charge carrier at these boundaries. Carrier concentration diminished with longer annealing time, and it was of the order of 10^{18}, this high value may be due to the presence of oxygen vacancies or excess of interstitial copper atoms as suggested by some authors.

Films prepared by annealing Al_2O_3/CuO/sapphire showed a higher resistance and sample annealed during 5 hours was out of the limits of the equipment employed. An increment of electrical resistivity and mobility is also observed with longer annealing times, however contrasting with the previous case, carrier concentration also increases.

III. Conclusions

This work presented a comparative study of $CuAlO_2$ thin film preparation by magnetron sputtering and systematically optimized the growth conditions for $CuAlO_2$ thin films.

$CuAlO_2$ thin films were successfully obtained by two different methods i.e. direct diffusion of CuO in sapphire and CuO/Al_2O_3 sandwich deposited on sapphire, followed by RTA. The $CuAlO_2$ thin films grown from CuO diffusion to sapphire showed better optical and electrical characteristics compared to those from CuO/Al_2O_3 sandwich on sapphire.

This material showed p-type conductivity and good transparency (~60%) making it promising for transparent electronic applications. Existing transparent conductors are mostly n-type materials, $CuAlO_2$ films with p-type conductivity open new applications possibilities. The highest electrical conductivity and charge carrier concentration obtained were of 1.01 $x10^{-1}$ $S \cdot cm^{-1}$ and 3.63 $x10^{18}$ cm^{-3}, respectively. These values are comparable to those reported in the literature, and the results obtained in this work indicate these values can be raised with proper control of post-deposition conditions.

Post-deposition parameters critically determine quality of films and resulting physical properties. Longer annealing time and slow cooling rates are necessary for proper phase formation, favoring higher electrical conductivity and optical transparency of the films.

Projections for future work

Improved electrical conductivity as well as optical transparency is required. Some of the suggested future research possibilities are:

Exploring different cooling rates, It is clear from the present investigation that cooling rates have a prominent effect on surface morphology and grain growth. Optimizing cooling rate will make it possible to achieve better transparency and electrical conductivity as they are much influenced by grains and grain boundaries.

Study electrical anisotropy, according to literature, the value of electrical conductivity measured along the c-axis is expected to be higher than into the ab perpendicular plane. Following the same procedure presented in this work, $CuAlO_2$ films could be grown with an orientation perpendicular to c-axis. For this purpose sapphire substrates with proper orientation should be used. The study of the electrical properties in different directions will lead to a better understanding of the electrical behavior of $CuAlO_2$.

Preparing P-n junctions, n-ZnO/p-$CuAlO_2$ heterojunction devices can be fabricated and characterized. P-n junctions constitute the basic unit for a wide variety of applications such as field emission transistors, rectifiers, solar cells, light emitting diodes, etc. Transparent p-n junctions could extend the existent applications market beyond its present limits.

References

[1] F.A. Benko and F.P. Koffyberg, J. Phys. Chem. Solids **45,** 57 (1984).

[2] H. Hahn and C. de Lorent, Z. Anorg. Allg. Chem., **279**, 281 (1955)

[3] D.B. Rogers, R.D. Shannon, C.T. Prewitt and J.L. Gillson, Inorg. Chem. **10**, 723 (1971).

[4] Y.J. Shin, J.H. Kwak and S. Yoon, Bull. Korean Chem. Soc. **18** 775 (1997).

[5] T. Ishiguro, A. Kitazawa and M. Kato, J. Solid State Chem. **40**, 170 (1981).

[6] B.U. Köhler and M. Jansen, Z. Anorg. Allg. Chem. **543**, 73 (1986).

[7] R. Yu, D. Tasi, R. Chu, C. Huang, and F. Shieu, J. Electrochem. Soc. **154**, H1014 (2007).

[8] M.A. Marquardt, N.A. Ashmore and D.P. Cann, Thin Solid Films **496,** 146 (2006).

[9] J. Tate et al., Phys Rev. B **80** 165206 (2009).

[10] M.S. Lee, T.Y. Kim and D. Kim, Appl. Phys. Lett. **79**, 2028 (2001).

[11] H. Yanagi, S. Inoue, K. Ueda, and H. Kawazoe, J. Appl. Phys. **88** 4159 (2000).

[12] H. Kawazoe, H. Yanagi, K. Ueda and H. Hosono, MRS Bull. August 2000 28.

[13] B. J. Ingram, T. O. Mason, R. Asahi, K. T. Park and A. J. Freeman, Phys. Rev. B: Condens. Matter. **64**, 155114 (2001).

[14] Y. Wang and H. Gong, Chem. Vap. Deposition **6,** 285 (2000).

[15] A.N. Banerjee, P.K. Gosh and K.K.Chattopadhyay, Sol. Energy Mater. Sol. Cells. **89**,75 (2005).

[16] G. Thomas, Nature **389,** 907 (1997).

[17] H. Kawazoe, M. Yasukawa, H. Hyodo, M. Kurita, H. Yanagi, and H. Hosono, Nature **389** 939 (1997).

[18] A.S. Reddy, H. Park, G.M. Rao, S. Uthannac and P.S. Reddy, J. Alloys Compd. **474**, 401 (2009).

[19] W. Lan et al., J. Mater. Sci. **44**, 1594 (2009).

[20] G. Dong, M. Zhang, X. Zhao, Y. Li and H. Yan, J. Cryst. Growth **311**,1256 (2009).

[21] A.N. Banerjee, R. Maity, C.K. Gosh and K.K.Chattopadhyay, Thin Solid Films **474,** 261 (2005).

[22] A. Buljan, P. Alemany and E. Ruiz, J. Phys. Chem. B **103**, 8060 (1999).

[23] X. Nie, S.-H. Wei and S.B. Zhang, Phys. Rev. Lett. **88** 066405 (2002).

[24] D.J. Aston et al., Phys. Rev. B, **72** 195115 (2005).

[25] R. Laskowski, N.E. Kristensen, P. Blaha, B. Palanivel, Phys. Rev. B, **79** 165209 (2009).

[26] A.N. Banerjee and K.K.Chattopadhyay, in *Reactive Sputter Deposition*, edited by D. Depla & S. Mahieu (Springer-Verlag, Berlin, 2008).

[27] J. Cai and H. Gong, J. Appl. Phys. **98**, 033707 (2005).

[28] A.N. Banerjee, P.K. Gosh, S. Das and K.K. Chattopadhyay, Physica B **370,** 264 (2005).

[29] J. Pellicer-Porres et al. Appl. Phys. Lett. **88,** 181904 (2006).

[30] S.P. Misra and A.C.D. Chaklader, J. Am. Ceram. Soc. **46,** 509 (1963).

[31] K.T. Jacob and C.B. Alcock, J. Am. Ceram. Soc. **58**, 192 (1975).

[32] Z. Deng, X. Fang, R. Tao, D. Li and X. Zhu, J. Alloys Compd., **466**, 408 (2008).

[33] M. Neumann-Spallart, S.P. Pai and R. Pinto, Thin Solid Films **515** 8641 (2007).

[34] R.E. Stauber, J.D. Perkins, P.A. Parilla and D.S. Ginley, Electrochem. Solid-State Lett. **2** (12) 654 (1999).

[35] K. Tonookaa, H. Bando, and Y. Aiura, Thin Solid Films **445,** 327 (2003).

[36] E.M. Alkoy and P.J. Kelly, Vacuum, **79**, 221 (2005).

[37] A.N. Banerjee, S. Kundoo, and K.K.Chattopadhyay, Thin Solid Films **440,** 5 (2003).

[38] A.N. Banerjee, S. Kundoo, and K.K.Chattopadhyay, Mat. Lett. **58,** 10 (2003).

[39] W. Lan, M. Zhang, G. Dong, Y. Wang and H. Yan, J. Mater. Res. **22**, (12) 3338 (2007).

[40] C.H. Ong and H. Gong, Thin Solid Films **445,** 299 (2003).

[41] J.H. Shy and B.H. Tseng, J. Phys. Chem. Solids **66**, 2123 (2005).

[42] J.H. Shy and B.H. Tseng, J. Phys. Chem. Solids **69**, 547 (2008).

[43] M.K. Singh, S. Dussan, G.L. Sharma and R.S. Katiyar, J. Appl. Phys., **104**, 113503 (2008).

[44] N. Tsuboi et al., J. Phys. Chem. Solids, **64** 1671 (2003).

[45] N. Tsuboi et al., Jpn. J. Appl. Phys. **46**, 351 (2007).

[46] N. Tsuboi et al., Jpn. J. Appl. Phys. **47**, 592 (2008).

[47] R. Yu, S. Liang, C. Lu, D. Tasi and F. Shieu, Appl. Phys. Lett. **90** 191117 (2007).

[48] H. Gong, Y. Wang and Y. Luo, App. Phys. Lett., **36**, 3959 (2000).

[49] Y. Wang et al., Mater. Sci. Eng., **85** 131 (2001).

[50] C. Bouzidi, H. Bouzouita, A. Timoumi and B. Rezig, Mater. Sci. Eng., B, **118,** 259 (2005)

[51] J.Y. Rim, S.A. Song and S.B. Park, Mat. Res. Soc. Symp. Proc., 703 v.6.9.1 (2002).

[52] K. Tonookaa, K. Shimokawaa, and O. Nishimurab, Thin Solid Films **411,** 129 (2002).

[53] S. Götzendörfer, C. Polenski, S. Ulrich and P. Löbmann, Thin Solid Films, **518**, 1153 (2009).

[54] L. Torkian L. and M.M. Amini, Mater. Lett. **63**, 587 (2009).

[55] D.S. Kim, S.J. Park, E.K. Jeong, H.K. Lee and S.Y. Choi, Thin Solid Films **515**, 5103 (2007).

[56] M. Ohashi, Y. Iida and H. Morikawa, J. Am. Ceram. Soc., **85**, 270 (2002).

[57] J. Pellicer-Porres et al. Phys Rev. B, **74,** 184301 (2006).

[58] J. Pellicer-Porres, A. Segura, and D. Kim. Semicond. Sci. Technol. **24,** 015002 (2009).

[59] R. Díaz Martínez, *Synthesis of $CuAlO_2$ thin films by Pulsed Laser Deposition.* M.S. Thesis, University of Puerto Rico – Mayagüez, 2009.

[60] S. Berg., T. Nyberg, and T. Kubart, in in *Reactive Sputter Deposition*, edited by D. Depla & S. Mahieu (Springer-Verlag, Berlin, 2008)

[61] W.D. Westwood in *Handbook of Plasma Processing Technology* edited by. S. Rossnagel, J. Cuomo and W.D. Westwood (Noyes Publication, New Jersey,1990).

[62] M. Ohring. *The Materials Science of Thin Films Deposition and structure,* 2nd.ed. (Academic Press, 2002).

[63] D. Depla, S. Mahieu and R. De Gryse in *Reactive Sputter Deposition*, edited by D. Depla & S. Mahieu (Springer-Verlag, Berlin, 2008).

[64] K. Koski, J. Hölsä, and P. Juliet, Surf. Coat. Technol. **116–119,** 716 (1999).

[65] R. E. Dinnebier and S. J. Billinge, *Powder Diffraction. Theory and Practice* (RCS, Cambridge, 2008).

[66] M. Ohring. *The Materials Science of Thin Films Deposition and structure,* (Academic Press, 1992).

[67] L. J. Van der Pauw, Phillips Research Reports **13**, 1 (1958).

[68] L. J. Van der Pauw, Philips Technical Review **20**, 220 (1959).

[69] Keithley Instruments Inc. *Low Level Measurements Handbook. 6th edition* (Keithley Instruments, Cleveland, 2009).

[70] Keithley Instruments Inc. *Model 7065 Hall Effect Card Instruction Manual* (Keithley Instruments, Cleveland,1989).

[71] D.K. Schroder, *Semiconductor Material and Device Characterization* 3rd.ed. (John Wiley & Sons, New Jersey, 2006).

[72] M. Fox, *Optical Properties of Solids* (Oxford University Press, New York, 2001)

[73] M. Grundmann, *The Physics of semiconductors* (Springer-Verlag, Berlin, 2006)

[74] C. Chu, H. Lu, C. Lo, C. Lai, C. and Y. Wang, Physica B **404,** 4831 (2009).

[75] T. Fujimura and S. Tanaka, Acta Mater. **46,** 3057 (1998).

[76] J.F. Wager, D.A. Keszler and R.D Presley, *Transparent electronics* (Springer, New York, 2008).

[77] A. Buljan, M. Llunell, E. Ruiz, and P. Alemany, Chem. Mater. **13**, 338 (2001).

[78] J. Tauc, MRS Bull. **3,** 37 (1968).